Stress level estimates in coated or uncoated silicon nanoparticles during lithiation

Guilherme Viana, Renaud Masson, Bruno Michel, Benoit Mathieu, Mihail Gărăjeu

Stress level estimates in coated or uncoated silicon nanoparticles during lithiation

Guilherme Viana[a], Renaud Masson[a,*], Bruno Michel[a], Benoit Mathieu[b], Mihail Garajeu[c]

[a] *CEA DES, IRESNE, DEC, SESC, Cadarache, 13108 Saint-Paul-lez-Durance, France*
[b] *CEA, DRT, LITEN, DEHT/SAMA, 38000 Grenoble, France*
[c] *Aix Marseille Université, CNRS, Centrale Marseille, LMA, F-13453 Marseille, France*

Abstract

This work is devoted to the modelling of the mechanical behavior of coated or uncoated silicon nanoparticles, which constitute the anode active material in some lithium ion batteries, during their first lithiation at room temperature. The lithiation process induces a large volume expansion of the particles and a high level of stresses, which can lead to the fragmentation of the particles. Several approaches are proposed in order to estimate the volume expansion and the stress levels experienced by the particles. An original semi-analytical small strain model is first presented, which adapts the solution proposed by Seck et al. (2018) of the elastic-viscoplastic composite sphere problem subjected to radial loading, to the lithiated particle problem, in particular by considering the variation of phases properties during lithiation. The lithium concentration in the silicon particle is given by a sigmoid function (called logistic function) in order to mimic the reaction front between the phases.The implementation of the approach using the Hencky strain tensor (Miehe et al. (2002)) is proposed to take into account the large strains experienced by the particles. A complete description of the formulation is provided and the advantages are discussed. The importance of the large strains model is established by comparing it with the small strain one concerning the predictions of the pushing-out effect and the size effect of particles on their internal stresses during lithiation. Comparisons between our simulations and experimental data from Tardif et al. (2017) measuring the operando strain experienced by the pristine silicon gives the yield stress of the lithiated silicon. In addition, carbon-coated silicon nanoparticles are finally studied. We develop original closed-form expressions to predict the maximal stresses experienced by the coating at the end of the lithiation. Those expressions are used to re-estimate the fracture stress of pyrolitic carbon, considering a critical review of both pyrolitic carbon and lithiated silicon elastic properties. Finally, the mechanical effect of the coating on silicon during lithiation is studied.

Keywords: Lithium ion batteries, Silicon particles, Lithiation, Finite Element, Large strains, Carbon coating

*Corresponding author
Email address: renaud.masson@cea.fr (Renaud Masson)

1. Introduction

Lithium ion batteries (LIBs) using silicon as the anode active material is a promising material for electronic equipment because of its high energy density. The graphite employed at the anode of LIBs has a theoretical capacity of $372\,\mathrm{mA\,h\,g^{-1}}$ (Stournara et al. (2012)) and undergoes volume changes up to 10% under intercalation reaction (Qi et al. (2010)). On the other hand, silicon has higher theoretical capacity of $4200\,\mathrm{mA\,h\,g^{-1}}$ and undergoes alloying reaction with lithium, which leads to much larger volume expansion (Chan et al. (2008)). A major issue for improving the performance of LIBs using silicon is understanding their degradation that leads to capacity fade. According to Xu et al. (2017), the main degradation mechanisms are i) silicon cracking and pulverization due to volume expansion of 300% of Si upon full lithiation ii) loss of electrical contacts between silicon and conductive material due to silicon contraction during delithiation and iii) formation of a thick solid electrolyte interface (SEI) layer. In our work, we focus in the study of the first degradation mechanism. Several *in situ* and *in operando* experimental techniques have been conducted in the past to understand the lithiation mechanisms. These studies have evidenced the formation of an inward advancing lithiation front separating two phases in which the lithium concentration changes drastically between them: a pure silicon core and a silicon lithium alloy outer shell. For initially crystalline particles (c-Si), the amorphous alloy formed during lithiation at room temperature is the $Li_{3.75}Si$, leading the particle to a high volume expansion of about 300 % (Liu et al. (2011)). *In situ* TEM studies revealed that lithiation of (c-Si) nanowires and (c-S) nanoparticles advances through the propagation of a lithiation reaction front of about 1 nm in width, that separates the two phases (Liu et al. (2012a); Chon et al. (2011) and McDowell et al. (2012)).

In order to study the mechanical consequences of lithiation, Tardif et al. (2017) used X-ray diffraction (XRD) to measure *in operando* the time evolution of the elastic strain experienced by the crystalline cores of spherical silicon nanoparticles under lithiation. *In situ* TEM experiment from Liu et al. (2012b) on crystalline silicon discovered a strong nanosphere size dependence regarding fracture. It was found a critical particle diameter of about 150 nm, below which the particles neither cracked nor fractured upon first lithiation. It was observed that the cracking arose owing to tensile hoop stresses in the lithiated shell. The stress reversal from compression to tension at the shell surface is attributed to the movement of the reaction front between the inner core of pristine Si and the outer shell and plasticity, generating a pushing out of the lithiated material. Indeed, some experiments led on silicon thin films evidenced clearly that the large deformation induced by lithiation can be accommodated by plastic flow (Chon et al. (2011); Sethuraman et al. (2010)). In that context, the carbon coating of the silicon nanoparticle is a way to mitigate its risk of failure during lithiation depending on its strength as reported in Li et al. (2016).

Besides experimental investigations, several numerical models, using semi-analytical or finite element approaches, have been proposed to understand the mechanics of silicon lithiation. Zhang et al. (2007) considered the diffusion equation (Fick's equation) with a constant diffusion coefficient coupled with a linear elastic mechanical model, the elastic moduli being homogeneous within the particle. The constant diffusion coefficient does not produce the expected sharp variation of lithium concentration at the reaction front. In addition, their results show that hoop stress is negative in the whole particle, contrary to experimental observations

highlighting a tension of the particle's periphery. Zhao et al. (2012a) proposed a core-shell model, the lithiated shell having a perfectly plastic model. Neglecting the thickness of the front and the elastic strains, an analytical solution was derived. Results show positive hoop stress attained in the particle periphery, showing the key role of the plastic deformation of the lithiated shell. Huang et al. (2013) developed an elastic-viscoplastic core-shell model, the sharp but continuous concentration variation of lithium being modelled by a logistic function. They solved numerically by a finite difference method this nonlinear problem and confirmed that the plastic yielding of the lithiated shell is mandatory to obtain tensile hoop stress in the particle periphery. The finite element method (FEM) method has also been extensively used in the field of mechano-chemistry. Guo and Jia (2021) used ABAQUS to propose the most complete core-shell model to our knowledge. Therefore and unlike the previous work of Huang et al. (2013), the variation of elastic properties due to silicon alloying was taken into account in their model. In addition, they also modelled the large strains of the shell by using an updated lagrangian approach and solving a nonlinear diffusion problem to model the radial penetration of lithium. They analysed the stresses evolution during lithiation. These models have also been applied to the study of coated nano-particle silicon inclusions. Based on experimental results, Li et al. (2016) highlighted that the carbon coating may have a deleterious effect on the integrity of the particle as they will break for diameters much lower than the ones measured on uncoated silicon particles. Even if their numerical investigations are based on questionable material data (it will be explained later), the numerical study reported in that contribution demonstrates clearly that if a radial crack appears in the carbon coating during the lithiation, the silicon particle will break. It is worth remarking at this stage that the effect of some important features of all those models (effect of the particle size on stresses, large versus small strains descriptions) on the numerical predictions have yet to be evaluated.

Even if considerable progress have been made to model the lithiation of silicon nanoparticles, their validation by comparison with experimental data remains largely perfectible. In this work, we propose a novel comparison between experimental results and a state-of-the-art mechanical model taking into account all the main ingredients existing in the literature such as plasticity of the outer shell, time evolution of the sharp lithiation front, variation of phases properties during lithiation and large transformation. The structure of the paper consists of four sections. In section 2, an original semi-analytical small strain mechanical lithiation model is presented. For this purpose, we use the solution proposed in Seck et al. (2018) of the elastic-viscoplastic composite sphere problem subjected to radial loading and extend this solution to the lithiated particle problem, in particular by considering a time varying core-shell with a finite thickness interface. Afterwards, a finite element model is also proposed, the large strains experienced by the particles being taken into account via the Hencky logarithmic strain (Miehe et al. (2002)). This approach, applied to our knowledge for the first time to this type of phenomena, has very appealing features that are described in detail. In section 3, the predictive abilities of our models are assessed (prediction of the pushing-out effect already shown is previous works) while some new features are studied such as the effect of the particle size on stresses. Therefore, we compare the predicted results with the ones derived with the infinitesimal strain approach to underscore the importance of large strain. Next, those models are compared to the experimental results provided by Tardif et al. (2017) and the yield stress of lithiated silicon is determined. In section 4, an original

closed-form expression of the maximal stresses experienced by the coating at the end of the lithiationis reported. We use this new expression to discuss the results obtained in Li et al. (2016) considering in particular the effect of the elastic properties of the lithiated silicon and the carbon coating on the fracture strength of the pyrolitic carbon. With these consolidated data, we finally study the mechanical effect of the coating during the lithiation process.

2. Modelling the lithiation of a silicon particle

2.1. Modelling the lithiation front at room temperature by a logistic function (Huang et al. (2013))

As seen in the introduction, the lithiation of silicon is a complex phenomenon and the diffusion process involves the formation of a lithiation front. Experimental in situ TEM measure has shown that the lithiation front size is about 1 nm (Liu et al. (2012a)). Nevertheless, other essential information needed for modeling the front such as its shape, exact thickness and lithium concentration distribution remains unknown. To circumvent this problem, qualitative solutions have been proposed to include the lithiation front in the mechanical context, allowing the estimation of stresses and geometry evolution of silicon nanoparticles. The main idea of those qualitative solutions is to generate a sharp lithium concentration profile with an arbitrary shape to represent the interface between a pure silicon core and an outer lithiated shell. We emphasize that those techniques do not represent the kinetics of lithiation front nor other phenomena such as lithiation locking (McDowell et al. (2012); Poluektov et al. (2019)). However, for a given front position, one may estimate the mechanical response of the silicon particle.

In the following, we consider a spherical silicon nanoparticle of initial radius r_0 in the case of isotropic lithiation. We note $r_c(t)$ the position of the lithiation front measured with respect to the center of the particle (considered as the origin of the coordinates). One existing method to represent the lithiation front is the use of a nonlinear diffusion equation where the diffusion coefficient is chosen as nonlinear form in order to create a drastic variation of concentration in each phase. This technique was used initially in Liu et al. (2011) and then in Yang et al. (2014) and Liu et al. (2012b). Despite widely applied, the nonlinear diffusion equation has some drawbacks. For example, it requires interface-tracking techniques to update front position and numerical problems arise from the diffusion coefficient singularity. Another existing strategy to represent the lithiation front is the use of the so called logistic equation. The logistic equation proposed by Huang et al. (2013) to describe spatial and temporal variation of concentration is:

$$\hat{c}(\boldsymbol{x},t) = \frac{1}{\left[1 + Qe^{-B(\|\boldsymbol{x}\| - r_c(t))}\right]^{1/\alpha}} \tag{1}$$

with $\boldsymbol{x}$ the position of a point in the particle measured from its center. The concentration ranges from 0 (pristine silicon) to 1 (full lithiated silicon). The lithium stoichiometry in the particle is given as $\chi = \chi_{shell}\,\hat{c}(\boldsymbol{x},t)$ with χ_{shell} being the lithium stoichiometry in the full lithiated silicon. The maximum value of χ_{shell} observed in experimental results is 3.75 (Liu et al. (2011)). The parameters Q, B and α are constants allowing to modify the shape of the equation (1), conveniently chosen aiming a sharp variation of concentration.

One advantage of using the logistic equation is that the concentration profile is given explicitly, including the barely known front shape: economy of theoretical hassle with no real loss of physical sense. This simplified representation is particularly well adapted to the Tardif et al. (2017) experiments studied in section 3. Indeed, the prescribed charging rate is chosen sufficiently low so that the lithium concentration in the lithiated part can be considered constant. Solving a diffusion problem including possible stresses effects is therefore not necessary in this particular case. Considering the mentioned advantages, the logistic front model is chosen in this work. In section 3, the position front will be simply given by the conservation of lithium atoms flowing inside the silicon nanoparticle through the measure of the specific capacity, as done in Tardif et al. (2017). This logistic function will be also used in section 4 when estimating the mechanical behaviour of coated silicon particle. Following Huang et al. (2013), Q and α are chosen as unity and B can be used to modify the logistic equation thickness. In order to generate a $e_f = 1$ nm lithiation front size, we use $B = 13 \times 10^9$.

The lithiation induces a volume expansion of the initial pure silicon nanoparticle. That expansion can be represented by a free chemical strain dependent on the lithium concentration. When the diffusion is isotropic, the chemical strain at a point $\boldsymbol{x}$ of the particle is (see Garcıa et al. (2004)):

$$\underline{\underline{\boldsymbol{\varepsilon}}}^c(\boldsymbol{x}, t) = \beta\, \hat{c}(\boldsymbol{x}, t)\, \underline{\underline{\boldsymbol{I}}} \tag{2}$$

with β the expansion coefficient and $\underline{\underline{\boldsymbol{I}}}$ is the identity second order tensor. For a crystalline particle and a small strain model (see subsection 2.2.2), $\beta = 0.6$ yields a 300% volume expansion as observed in experimental analysis. The chemical strain is treated similarly to a temperature induced strain and the lithium concentration drives the differential swelling within the particle.

2.2. Mechanics of lithiation

In this section, we introduce the general aspects and formulation of the mechanical problem in lithiation considering small and large strain approach. In our model, anisotropic effects related to the shape of the lithiation front as well as the anisotropy related to the elastic properties of the crystalline particles are neglected. As explained above, the chemical deformation is applied analogously to the thermal problem where the concentration of lithium replaces the temperature and the thermal expansion coefficient is replaced by a chemical expansion coefficient.

2.2.1. Material constitutive laws

Reference	*Technique*	$E_{Si}\,(GPa)$	$E_{a-Li_{3.75}Si}\,(GPa)$
Shenoy et al. (2010)	atomistic simulations	175 (c-Si) [111]	40
Hertzberg et al. (2011)	nanoindentation	92 (a-Si)	12
Kushima et al. (2012)	*in situ* tension /atomistic simulations	180/173 (c-Si) [111]	7.9/33.5
Qi et al. (2014)	atomistic simulations	96 (a-Si)	41
Berla et al. (2015)	nanoindentation	104.6 (a-Si)	41

Table 1: Young modulus of silicon (E_{Si}) and lithiated silicon ($E_{a-Li_{3.75}Si}$) at room temperature.

Several experimental and numerical studies were performed to determine the properties of silicon and lithiated silicon. It is shown in those studies an important variation of the Young modulus between a-Si, c-Si and the alloy a-$Li_{3.75}Si$. In Table 1, we reported the Young modulus either measured using different experimental techniques or calculated by atomistic simulations. Concerning the Young modulus of the amorphous lithiated silicon, the value of approximately 40 GPa has been identified in most of the references, except in Hertzberg et al. (2011) and Kushima et al. (2012), in which the Young modulus is lower (dozen of GPa). Because the fully lithiated silicon alloy melts at much higher temperatures than the pure lithium, Berla et al. (2015) claimed that the stiffness of the fully lithiated silicon must be considerably larger than the Young modulus of pure lithium that is approximately 8 GPa (Robertson and Montgomery (1960); Tariq et al. (2003)). Following that argument, the Young modulus of the fully lithiated silicon alloy considered in this work is 40 GPa. Concerning the Poisson ratio, Shenoy et al. (2010) found the value of 0.22 for fully lithiated silicon. Then, the bulk and shear modulus for the full lithiated silicon used in this work are respectively $\kappa_S = 23.8$ GPa and $\mu_S = 16.4$ GPa.

Crystalline silicon has a cubic symmetry. Shenoy et al. (2010) found via atomistic simulations a Young modulus of 175 GPa in the [111] crystallographic direction, which is consistent with the 180 GPa measured experimentally by Kushima et al. (2012). In this work, we adopt an isotropic elasticity tensor using the arithmetic mean of the Reuss and Voigt bounds of the effective bulk and shear moduli of polycrystalline silicon using the single crystal elastic tensor from Shenoy et al. (2010). It yields an average value for the shear and bulk moduli respectively as $\mu_0 = 64.51$ GPa and $\kappa_0 = 102.5$ GPa (corresponding to an average value of $E_0 = 160$ GPa and $\nu_0 = 0.24$). The average value of the Young modulus is consistent with 162 GPa found by Hopcroft et al. (2010).

Shenoy et al. (2010) also found that average elastic moduli decreases in an approximately linear manner with increasing lithium concentration, leading to a significant elastic softening in lithiated silicon. We then define the elastic properties depending linearly (Shenoy et al. (2010)) on lithium stoichiometry χ ($0 \leq \chi \leq 3.75$) as following:

$$\mu = \mu_0 \left(1 - \frac{\chi}{3.75}\right) + \mu_S \left(\frac{\chi}{3.75}\right) \tag{3}$$

$$\kappa = \kappa_0 \left(1 - \frac{\chi}{3.75}\right) + \kappa_S \left(\frac{\chi}{3.75}\right) \tag{4}$$

Such as the elastic properties, the yield stress in the lithiated silicon is dependent on the lithium content and decreases with it. The yield stress of pure crystalline silicon is around 12 GPa (Yang and Qu (2019)). The yields stress of amorphous lithiated silicon changes non linearly and drops significantly with respect to lithium stoichiometry χ, from 5.4 GPa for $Li_{0.25}Si$ to 2.5 GPa for $Li_{1.0}Si$ (Cui et al. (2012), Wang and Chew (2016)). Regarding the full lithiated alloy $Li_{3.75}Si$, the range of value of the yield stress reported in the literature is $0.4 - 1.5$ GPa (Chon et al. (2011); Zhao et al. (2011, 2012b); Pharr et al. (2014)). In our model, the yield stress is taken different in the pristine silicon (12 GPa) and the lithiated shell (0.45 GPa). As it has been shown to decrease abruptly with the lithium concentration, the yield stress inside the reaction front is taken constant and equal to the one of the fully lithiated silicon shell. In this work, we consider the yield stress of the lithiated shell being $\sigma_Y = 0.45$ GPa, value that best match experimental results as it will be detailed in section

3.3. For a silicon particle, the total strain rate can be written as (Pharr et al. (2014)):

$$\underline{\underline{\dot{\varepsilon}}}(\boldsymbol{x},t) = \underline{\underline{\dot{\varepsilon}}}^{c}(\boldsymbol{x},t) + \underline{\underline{\dot{\varepsilon}}}^{e}(\boldsymbol{x},t) + \underline{\underline{\dot{\varepsilon}}}^{vp}(\boldsymbol{x},t) \tag{5}$$

where the viscoplastic strain rate is written as (Seck et al. (2018)):

$$\underline{\underline{\dot{\varepsilon}}}^{vp}(\boldsymbol{x},t) = 3\,\underline{\underline{\boldsymbol{s}}}(\boldsymbol{x},t)\,\frac{\partial w}{\partial \widetilde{\sigma}}(\widetilde{\sigma}) \tag{6}$$

with $\underline{\underline{\boldsymbol{s}}} = \underline{\underline{\boldsymbol{\sigma}}} - \sigma_m \underline{\underline{\boldsymbol{I}}}$ the deviatoric stress tensor and $\sigma_m = tr(\underline{\underline{\boldsymbol{\sigma}}})/3$ the mean stress. The parameter w is a dissipation potential. For Norton's law, used in Huang et al. (2013) and Seck et al. (2018), function of $\widetilde{\sigma}$, $\widetilde{\sigma} = \sigma_{eq}^2$, this potential is:

$$w(\widetilde{\sigma}) = \frac{\dot{\varepsilon}_0\,\sigma_Y}{\frac{1}{m}+1}\left(\frac{\widetilde{\sigma}}{\sigma_Y^2}\right)^{\frac{\frac{1}{m}+1}{2}} \tag{7}$$

with $\sigma_{eq} = \sqrt{3\,\underline{\underline{\boldsymbol{s}}} : \underline{\underline{\boldsymbol{s}}}/2}$ is the von Mises equivalent stress. The viscoplastic constants are the effective strain rate, $\dot{\varepsilon}_0$, the yield stress σ_Y and m is the sensitivity to the strain rate. Few works have studied these strain rate effects. Pharr et al. (2014) measured experimentally a strain rate that is much higher ($10^{-3}\,s^{-1}$) than the one considered in section 3.3 ($10^{-8}\,s^{-1}$). Due to lack of data on this point, in this work the value of m is taken vanishingly small such as in Huang et al. (2013), then one can approximate the rate-independent behaviour to a perfectly plastic material. Nevertheless, in the following we conserve the viscoplastic formulation as it can be explored in future works. Taking into account all ingredients, the constitutive law can be written as:

$$\begin{aligned}\underline{\underline{\dot{\varepsilon}}}(\boldsymbol{x},t) &= \left(\frac{\dot{\sigma}_m(\boldsymbol{x},t)}{3\,\kappa(\boldsymbol{x},t)} - \frac{\sigma_m(\boldsymbol{x},t)\,\dot{\kappa}(\boldsymbol{x},t)}{3\kappa^2(\boldsymbol{x},t)} + \dot{\varepsilon}^{c}(\boldsymbol{x},t)\right)\underline{\underline{\boldsymbol{I}}} \\ &+ \frac{\underline{\underline{\dot{\boldsymbol{s}}}}(\boldsymbol{x},t)}{2\mu(\boldsymbol{x},t)} + \left(3\,\frac{\partial w}{\partial \widetilde{\sigma}}(\widetilde{\sigma}) - \frac{\dot{\mu}(\boldsymbol{x},t)}{2\mu^2(\boldsymbol{x},t)}\right)\underline{\underline{\boldsymbol{s}}}(\boldsymbol{x},t)\end{aligned} \tag{8}$$

As the elastic properties depends on the lithium stoichiometry, they are also function of space and time.

2.2.2. Small strain semi-analytical model

The small strain semi-analytical model proposed in this work consider all the ingredients such as elastic properties variations with the lithium concentration, viscoplasticity and lithiation front size via the logistic equation. It is an extension of the composite model of a sphere subjected to a radial loading in the case of elasto-viscoplastic constituents developed by Seck et al. (2018). We write the equations for each constituent of the composite material. Using equation (8), boundary conditions (free outer external border) and equilibrium equation are written considering a 1D spherical problem. Consistently with the isotropic lithiation and the isotropic behaviour of the phases, we adopt spherical coordinates (r, θ, ϕ) and we derive a system of nonlinear equations to be solved for signed equivalent stress $\hat{\sigma}(r,t) = (\sigma_{\theta\theta} - \sigma_{rr})/\sigma_Y$ and for the normalized displacement $\hat{u}(r,t) = u/r$ (details given in Appendix A):

$$\frac{1}{\hat{\mu}}\frac{\partial \hat{\sigma}(r,t)}{\partial t} - \frac{\dot{\hat{\mu}}(r,t)}{\hat{\mu}^2(r,t)}\hat{\sigma}(r,t) + 3\dot{\varepsilon}_0\left(\hat{\sigma}^2(r,t)\right)^{\frac{\frac{1}{m}-1}{2}}\hat{\sigma}(r,t) + 2r\frac{\partial}{\partial t}\left(\frac{\partial \hat{u}(r,t)}{\partial r}\right) = 0. \tag{9}$$

$$-\hat{\sigma}(r,t)+\frac{3r}{2}\hat{\kappa}(r,t)\frac{\partial\hat{u}(r,t)}{\partial r}+\frac{9}{2r^3}\int_0^r\frac{\partial\hat{\kappa}(x,t)}{\partial x}(x,t)\,x^3\hat{u}(x,t)\,dx \\ +\frac{27}{2r^3}\hat{F}(r,t)-\frac{9}{2r^2}\frac{\partial\hat{F}(r,t)}{\partial r}=0. \tag{10}$$

with

$$\hat{\kappa}(r,t)=\frac{\kappa(r,t)}{\sigma_Y}\quad \hat{\mu}(r,t)=\frac{\mu(r,t)}{\sigma_Y}\quad \hat{F}(r,t)=\int_0^r\hat{\kappa}(x,t)\,\varepsilon^c(x,t)\,x^2\,dx \tag{11}$$

The term $\hat{F}(r,t)$ includes the chemical strain. The main difference this solution compared to the one established in Seck et al. (2018) is the existence of an additional term including the spatial derivation of normalized bulk modulus in the spatial integration in equation (10). In addition, the interface between the lithiated and pristine silicon (silicon core) is given as a continuum function (logistic) with a finite thickness. That additional term does not allow one to obtain a single differential equation with respect to $\hat{\sigma}$ (with analytical solution in some particular cases) such as in Seck et al. (2018). The solution of the system is carried out by adopting the finite difference method (details given in Appendix C) and the implicit Euler scheme in the equation (9). Boundary conditions for the silicon particle are $u(0,t)=0$, $\sigma_{rr}(r_0,t)=P_c(t)$ (with the function $P_c(t)$ being zero in the case of free outer boundary condition) and $\hat{\sigma}(0,t)=0$ (this last condition is shown using the equation (10) when $r\to 0$, assuming that $\varepsilon_{rr}(r,t)=\frac{\partial u}{\partial r}(r,t)$ is a continuous differentiable function of r). If the elastic properties do not depend on the lithium concentration, the 2×2 system of nonlinear equations reduces to a nonlinear equation:

$$\hat{\sigma}(r,t)+\frac{\dot{\varepsilon}_0}{2\hat{\eta}}\,\hat{\sigma}(r,t)^{\frac{1}{m}}=\frac{-r}{3\hat{\eta}}\frac{\partial}{\partial r}\left(\frac{3}{r^3}\int_0^r\dot{\varepsilon}^c(x,t)\,x^2\,dx\right). \tag{12}$$

with $\hat{\eta}=\frac{3\hat{\kappa}+4\hat{\mu}}{18\hat{\kappa}\hat{\mu}}$. This solution is significantly simpler compared to the solution proposed in Huang et al. (2013) which also reduces to a scalar equation (on the velocity field) but at the cost of an estimation by an explicit time integration method of the radial distribution of plastic deformation. Moreover, in Huang et al. (2013) a shooting method was implemented to enforce the velocity field solution to respect the free outer boundary condition. The fact that the silicon nanoparticles present an increase of volume up to 300% during lithiation may question the use of a model based on the assumption of small strains. This is the reason why a numerical modeling of the silicon particle in the context of finite strain is proposed in the following section.

2.2.3. Large strain approach using the finite element method

Large strain approach has been already considered for the silicon lithiation modeling in several works. A common approach (Bower et al. (2011)) is the use of the multiplicative decomposition of the total deformation into elastic, chemical and plastic part as:

$$\underline{\underline{\boldsymbol{F}}}=\underline{\underline{\boldsymbol{F}}}^e\cdot\underline{\underline{\boldsymbol{F}}}^p\cdot\underline{\underline{\boldsymbol{F}}}^c \tag{13}$$

with $\underline{\underline{\boldsymbol{F}}} = \underline{\underline{\boldsymbol{I}}} + \nabla \boldsymbol{u}$ the deformation gradient tensor. Xu and Zhao (2016) considered the Green-Lagrange tensor as strain measure modeling a three-dimensional spherical Si particle using COMSOL multiphysics. Poluektov et al. (2018) considered the multiplicative decomposition of the total deformation formulation in one-dimensional modeling of the chemical reaction between lithium ions and silicon particle. Jia and Li (2016) used the eulerian rate-form finite-strain for modeling the two-step lithiation of a-Si in Abaqus. Yang et al. (2014) also considered the eulerian formulation for modeling the lithiation of nanowires. Guo and Jia (2021) used the updated Lagrangian approach via Abaqus to account for large nonlinear geometrical changes induced by lithiation.

In this work, we propose an accurate finite element large strain model. Compared to some of the large strain approaches cited above, the formulation of the proposed model is reported in full details in this section. We consider the large strain approach via the Hencky logarithmic strain tensor as proposed by Miehe et al. (2002). The equilibrium of the mechanical problem is solved in the updated coordinates of the particle and reads $\nabla \cdot \underline{\underline{\boldsymbol{\sigma}}} = \boldsymbol{0}$. The boundary condition reads $\underline{\underline{\boldsymbol{\sigma}}}.\boldsymbol{n} = \boldsymbol{0}$ with $\boldsymbol{n}$ the normal vector at the (updated) outer free boundary. One advantage of applying the Hencky tensor is the re-usability of the formalism used to build constitutive equations in the framework of the small strain theory in order to solve the material behaviour equation. With the Hencky strain tensor, the additive split of the logarithmic strain into chemical expansion and mechanical parts gives an accurate assessment of the volume conservation as the multiplicative decomposition given in (13). In addition, the logarithmic strain is, as the Green Lagrange tensor, invariant with respect to rigid body rotation. The Hencky strain tensor is defined as:

$$\underline{\underline{\boldsymbol{\varepsilon}}}_{log} = \frac{1}{2} \log(\underline{\underline{\boldsymbol{F}}}^T \cdot \underline{\underline{\boldsymbol{F}}}) \tag{14}$$

Considering the decomposition of $\underline{\underline{\boldsymbol{F}}}$ in mechanical and chemical parts, the logarithmic chemical strain tensor writes $\underline{\underline{\boldsymbol{\varepsilon}}}^e_{log} = \log(\underline{\underline{\boldsymbol{F}}}^c)$ for an isotropic chemical dilatation. In accordance with equation (2), $\underline{\underline{\boldsymbol{F}}}^c = (1 + \beta\hat{c})\underline{\underline{\boldsymbol{I}}}$ and $\beta = 0.6$ in order to have 300% of volume increase at the end of the lithiation as observed in experimental analysis. To ensure the conservation of the mechanical power, we refer to the approach proposed by Miehe et al. (2002) with the stress tensor $\underline{\underline{\boldsymbol{T}}}$ being the work-conjugate of the Hencky strain tensor.

The transfer of the dual stress tensor to the Cauchy stress tensor, needed for the equilibrium resolution, is described in Figure 1 by the colored arrows. We note the variables at the final time of the constitutive equation integration step with the lower index 1. The Cauchy stress $\underline{\underline{\boldsymbol{\sigma}}}_1$ is determined in two steps. In the first step (step I in Figure 1), the second Piola-Kirchhoff tensor is computed as $\underline{\underline{\boldsymbol{S}}}_1 = 2\underline{\underline{\boldsymbol{T}}}_1 : \frac{\partial \underline{\underline{\boldsymbol{\varepsilon}}}_{log(1)}}{\partial \underline{\underline{\boldsymbol{C}}}_1}$. That operation corresponds to the inverse of the stretch part of the transformation $\underline{\underline{\boldsymbol{F}}}_1$. In the second step (step II in Figure 1), in order to compute the true Cauchy stress, the relation $\underline{\underline{\boldsymbol{\sigma}}}_1 = \frac{1}{J_1}\underline{\underline{\boldsymbol{F}}}_1 \cdot \underline{\underline{\boldsymbol{S}}}_1 \cdot \underline{\underline{\boldsymbol{F}}}_1^T$ is applied and it corresponds to the complete transformation $\underline{\underline{\boldsymbol{F}}}_1$ (stretch and rotation). We remark that for our particular case of the 1D spherical isotropic mechanical problem, the rotation part is null. Based on the Hencky strain approach, the parameters of the law $\underline{\underline{\boldsymbol{T}}} = f(\underline{\underline{\boldsymbol{\varepsilon}}}_{log})$ have to be identified using an interpretation of mechanical tests results through the Hencky strain formalism. In our case this process is not possible because we do not have available

classical mechanical tests involving large chemical strain phenomena [1]. In order to circumvent this problem, we propose an indirect estimation of the dual stress tensor based on a pseudo Cauchy stress tensor denoted by $\underline{\underline{\boldsymbol{\sigma}}}^*$ that verifies the constitutive law in the eulerian framework given by:

$$\dot{\underline{\underline{\boldsymbol{\sigma}}}}^* = \mathbb{E} : \left(\dot{\underline{\underline{\boldsymbol{\varepsilon}}}} - \dot{\underline{\underline{\boldsymbol{\varepsilon}}}}^c - \dot{p}\,\underline{\underline{\boldsymbol{n}}} \right) \tag{15}$$

with $\mathbb{E}$ being the fourth order elastic tensor, $\dot{\underline{\underline{\boldsymbol{\varepsilon}}}}^e = \dot{\underline{\underline{\boldsymbol{\varepsilon}}}} - \dot{\underline{\underline{\boldsymbol{\varepsilon}}}}^c - \dot{p}\,\underline{\underline{\boldsymbol{n}}}$ the elastic strain rate, $\dot{p}$ the plastic strain rate and $\underline{\underline{\boldsymbol{n}}}$ the unity normal tensor to the yield surface given by:

$$\underline{\underline{\boldsymbol{n}}} = \frac{3\,\underline{\underline{\boldsymbol{s}}}^*}{2\,\sigma^*_{eq}} \tag{16}$$

with σ^*_{eq} the equivalent von Mises stress and the plasticity criterion reads $\sigma^*_{eq} - \sigma_Y \leq 0$ for the perfect plastic material. The deviatoric part of the pseudo Cauchy stress is $\underline{\underline{\boldsymbol{s}}}^*$. During the integration step, the increment of plastic strain Δp and the increment of elastic strain $\Delta\underline{\underline{\boldsymbol{\varepsilon}}}^e$ are computed via the Euler implicit method for the integration of the ordinary differential equation (15). After the integration, the pseudo Cauchy stress checks $\underline{\underline{\boldsymbol{\sigma}}}^*_1 = \mathbb{E} : \underline{\underline{\boldsymbol{\varepsilon}}}^e_{log(1)}$, with $\underline{\underline{\boldsymbol{\varepsilon}}}^e_{log(1)}$ being the elastic logarithmic strain tensor. Finally, we compute the dual stress as $\underline{\underline{\boldsymbol{T}}}_1 = J_1\,\underline{\underline{\boldsymbol{\sigma}}}^*_1$. That equation is derived in the case of a spherical 1D problem in which $\underline{\underline{\boldsymbol{F}}}$ is a diagonal tensor (Helfer (2015)). The large strain method presented here is implemented in the finite element software Cast3M (http://www-cast3m.cea.fr/index.php) thanks to the MFront tool (Helfer et al. (2020)), both open source softwares. The latter solves the implicit integration of the constitutive law and derives, with the finite transformations, the Cauchy stress tensor needed for the updated Lagrangian equilibrium formulation in Cast3M.

3. Stresses experienced by spherical particles under lithiation, comparison to experiments

In the first part of this section, the internal stresses and the dimensional evolution of a crystalline silicon particle are evaluated considering small and large strain approaches and elastic and elastoplastic models. In the second part, we analyse the particle size effect on stress and radius evolution by fixing the front size as 1 nm, value observed in experimental results as discussed previously. We consider particles of size (diameter) 10, 20 and 200 nm. Particles of those dimensions were fabricated for experimental study (Li et al. (2016); Luo et al. (2016); Tardif et al. (2017)). Finally, in the last part of this section, a comparison with experimental results of particle deformation is performed.

We consider that the lithiation front position (in the first and second parts of this section) is chosen to be a linear normalized function of time, i.e, at $t = 1$, the particle is fully lithiated. In addition, we use the state of charge (SOC) which is defined at a given time t as $SOC(t) = 3r_0^{-3}\int_0^{r_0} c(r,t)r^2dr$ to compute the level of lithiation with respect to the initial configuration (Jia and Li (2016)). When SOC = 0, the particle is uncharged and when SOC = 100 %, we have the fully-charged state. In the third part of this section,

[1] We mean by classical mechanical test the one in which the load/displacement curve is measured.

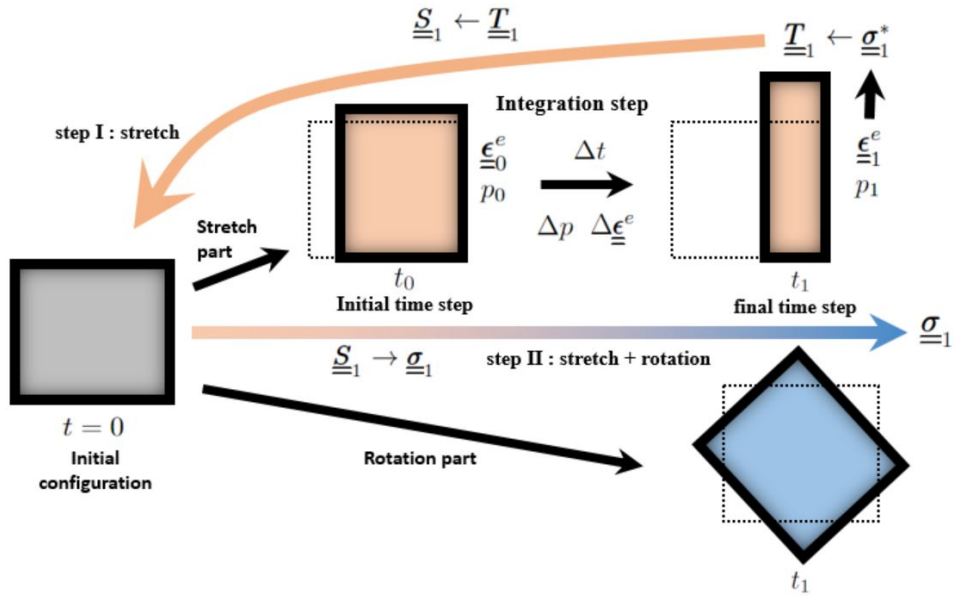

Figure 1: Scheme of the large strain method proposed in this work. The top part illustrates the stretch transformation of the material while the bottom part the rotation transformation. The transformation of the dual stress tensor $\underline{\underline{\boldsymbol{T}}}_1$ in the second Piola–Kirchhoff stress tensor $\underline{\underline{\boldsymbol{S}}}_1$ is indicated by the beige line. The transformation of the second Piola–Kirchhoff stress tensor in Cauchy stress tensor $\underline{\underline{\boldsymbol{\sigma}}}_1$ is indicated by the beige/blue line.

the lithiation front evolution is determined through experimental data. Because the one-dimensional spherical model is not available in MFront, we solve a 2D axisymmetric problem with spherical symmetry in the finite element large strain approach. The spherical particle geometry is represented by a thin circular sector with axisymmetric boundary conditions and its radial edges are divided in 400 uniform elements. In the small strain approach a 1D radial mesh with the same number of elements is considered. The material properties as well as the front size used in this section are shown in Table 2. In this work we consider the elastic properties of a crystalline silicon particle, which is consistent with the comparison with experimental results in section 3.3.

$E_0\,(GPa)$	$E_S\,(GPa)$	front size (nm)	ν_0	ν_S	$\sigma_Y(GPa)$
160	40	1	0.24	0.22	0.45

Table 2: Data used for simulations (isotropic elastic properties for crystalline silicon). The indexes 0 and S denote respectively the crystalline pristine silicon and the lithiated silicon.

3.1. Pushing out effect

In Figure 2, we plot the radial, tangential and equivalent stress field in an elastoplastic crystalline silicon particle, at the end of lithiation, for a 20 nm diameter particle. We observe that the outer boundary of the particle is submitted to a tensile hoop stress exactly equal to the yield stress value in the lithiated shell. That phenomena is called the pushing out effect because the lithiated silicon behind the lithiation front pushes the lithiated shell outwards during lithiation, inducing a tension in the tangential direction. In radial direction,

the particle is entirely in compression. Those results are in agreement with experimental observations as well as with others numerical results from Huang et al. (2013) and Jia and Liu (2016). In addition, we observe from the equivalent stress (σ_{eq}) that the entire lithiated region is in the plastic regime. In order to compare elastoplastic and pure elastic solutions (for a 20 nm diameter particle), we plot in Figure 3(a) the evolution of the normalized hoop stress with respect to the state of charge at the free outer boundary of the particle (in the lithiated shell). We observe that in the linear elastic case, the hoop stress is always negative during lithiation and reaches its maximum compression at around 10% of state of charge and vanishes at the end of lithiation. On the other hand, the hoop stress in the elastoplastic case is negative during the beginning of lithiation and then becomes positive. We observe that both plateau in compression and tension are consistent with the yield stress threshold $\sigma_Y = |\sigma_{rr} - \sigma_{\theta\theta}|$ with $\sigma_{rr}(r_0, t) = 0$. The absolute maximum hoop stress value is higher in the elastic case, 40 GPa, while 0.45 GPa (yield stress) in the plastic case. The compression to tension evolution of hoop stress observed in our calculations in the plastic case is qualitatively in good agreement with the results presented in the references Jia and Li (2016) and Jia and Liu (2016),

We plot in Figure 3(b) the normalized stress field for elastic and elastoplastic cases when $SOC = 45\%$ (the silicon core - in the region $r/r_0 \leq 0.3$ in the elastoplastic particle - is in hydrostatic stress state). This intermediate state of lithiation reinforces the strong effect of the plastic flow on the stress distribution in the particle. Thus, we observe that in the linear elastic case, the radial stress is positive in the whole particle, whereas it is negative in the plastic case. Likewise, the silicon core is in hydrostatic tension in the elastic case whereas in compression in the plastic case.

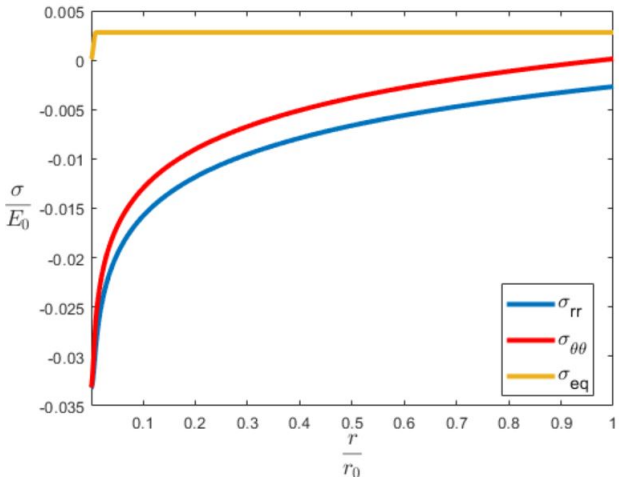

Figure 2: Normalized stress distribution at the end of lithiation of an elastoplastic particle using the large strain approach (the original diameter of the particle equals 20 nm, material data reported in Table 2). The final particle radius is 1.6 times bigger the initial radius, which is consistent with the volume increase expected (300%).

In Figure 4(a), we compare radial and hoop stress field in the case of small strain and large strain approaches for a 20 nm diameter particle, when $SOC = 45\%$. For the small strain case, we plot the stress field with respect to the initial configuration while for the large strain approach the deformed configuration is considered. In both cases, the silicon core

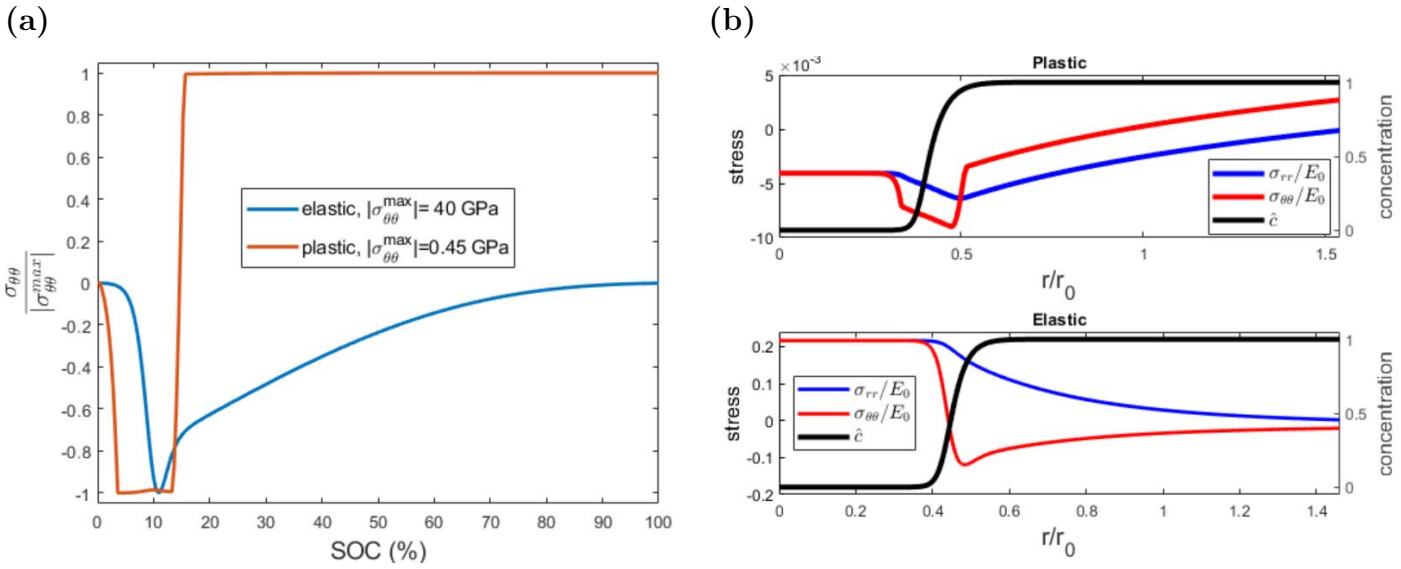

Figure 3: Effect of the plastic yielding of the lithiated silicon on the model predictions (large strain approach, the diameter of the particle equals 20 nm, material data reported in Table 2) : (a) evolution of the hoop stress at the outer boundary of the particle as a function of the state of charge (b) radial distribution of stresses and concentration profile when $SOC = 45\%$.

$(r/r_0 \leq 0.3)$ is under hydrostatic compressive stress. We observe that the compressive stress state in the silicon core is higher in the case of large strain approach (the evolution of the core elastic strain during lithiation will be discussed in detail in the next part of this section). This can be explained by the fact that the update of radius in the lithiated region in the large strain approach generates a bigger shell applying a pressure in the silicon core, whereas in the small strain case the geometry variation is not considered. In both cases, in the lithiated silicon, we observe that particle is in maximum compression in the tangential and radial direction just behind the silicon core. Hoop stress turns to tension towards the periphery of the particle and reaches its maximum value at the free edge similarly for the small and large strain models. In Figure 4(b) the evolution of the particle radius with respect to the state of charge is depicted in small and large strain cases. We found that the infinitesimal strain approach underestimates the particle radius during lithiation however at the end of the lithiation the radius is similar and it is controlled by the expansion coefficient, as discussed in section 2.2.

3.2. Particle size effect

In this part, the elastoplastic large strain model is considered and we study the particle size effect on the mechanical response during lithiation. In Figure 5, we plot the evolution of the updated particle normalized external radius (r_e/r_0) with respect to the state of charge and for different particle sizes. Three particle diameters, 200 nm, 20 nm and 10 nm are considered and we remark that the evolution is similar for all particles. This is owing to the fact that the expansion coefficient controls the volume expansion in the lithiated shell and is constant regardless the particle size. The small variation observed in Figure 5 is due to the different relative front size with respect to the particles diameters, which is small (0.5%, 5% and 10% respectively for a 200 nm, 20 nm and 10 nm particle). In Figure 6, we plot the stress fields

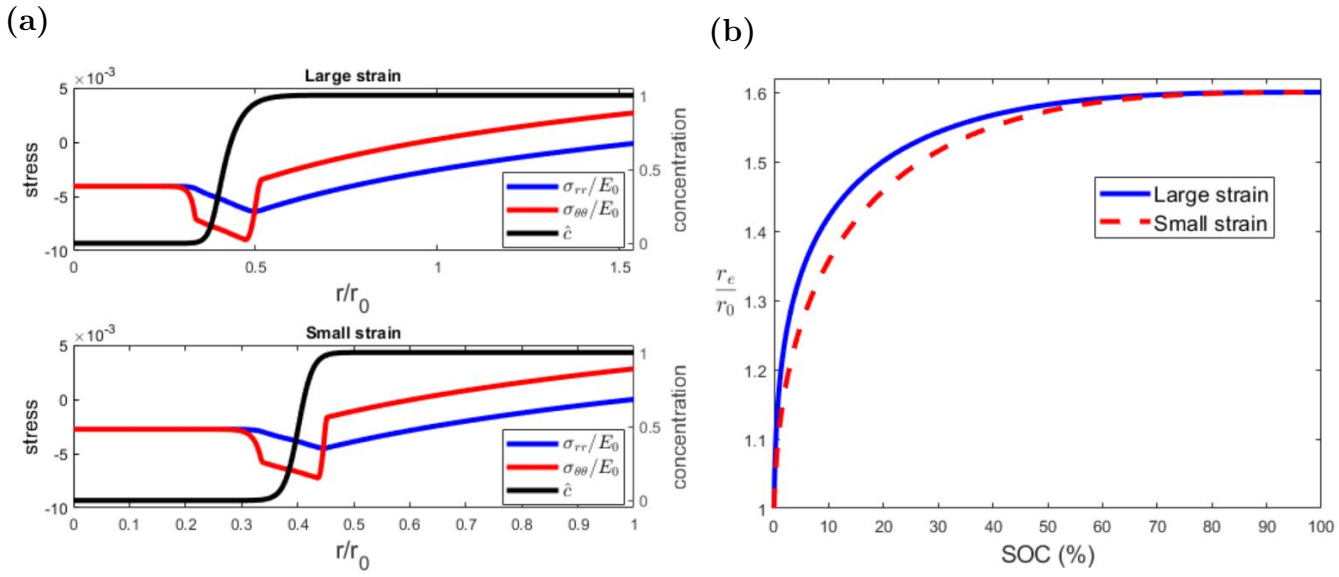

Figure 4: Comparison of small strain and large strain approaches (elastoplastic model, the diameter of the particle equals 20 nm, material data reported in Table 2) : (a) radial distribution of stresses and concentration profile when $SOC = 45\%$, predicted by elastoplastic model (b) evolution of the particle radius with respect to the state of charge.

when $SOC = 45\%$. Whatever the particle size is, the silicon core is always in hydrostatic stress state (region in which the radial and hoop stress are constant). In addition, we observe that the stress distribution towards the periphery does not depend on the particle size, the hoop stress being as expected positive and equal to the yield stress at the outer boundary. Nevertheless, we observe that the stress in the silicon core is very dependent on the particle size. For example, for a 10 nm diameter particle, the hydrostatic compression in the silicon core is in absolute values about 2.3 and 4 times lower than the particles of diameters 20 nm and 200 nm respectively. These results are consistent with experimental observations of Liu et al. (2012b). They revealed that silicon nanoparticles fracture occurs above a limit size of 150 nm. Appropriately, considering that the fracture is driven by elastic energy, our results shows that the elastic energy density increases with respect to the particle size, in particular in the silicon core. Finally, we also reveal that the stress field in the fully lithiated particle is independent of the particle size (the stress field is given in Figure 2).

3.3. Comparison with the experimental data provided by Tardif et al. (2017)

Several experimental works have been conducted in order to measure the stress and strain during lithiation of metallic anode materials such as silicon (Chon et al. (2011); Pharr et al. (2014); Sitinamaluwa et al. (2017); Choi et al. (2015)) and germanium (Cortes et al. (2018); Al-Obeidi et al. (2015)). Concerning specifically silicon nanoparticle, Tardif et al. (2017) used X-ray diffraction (XRD) to study in Operando mean deformation of the silicon core of a system of silicon crystalline particles in a soft electrolyte medium (for that reason we can assume free boundary condition at the outer surface of the particles). Diffraction intensity, scattering vector and specific capacity were measured during two lithiation-delithiation cycles at low charging rate, so that the lithium concentration in the lithiated phase is constant. The

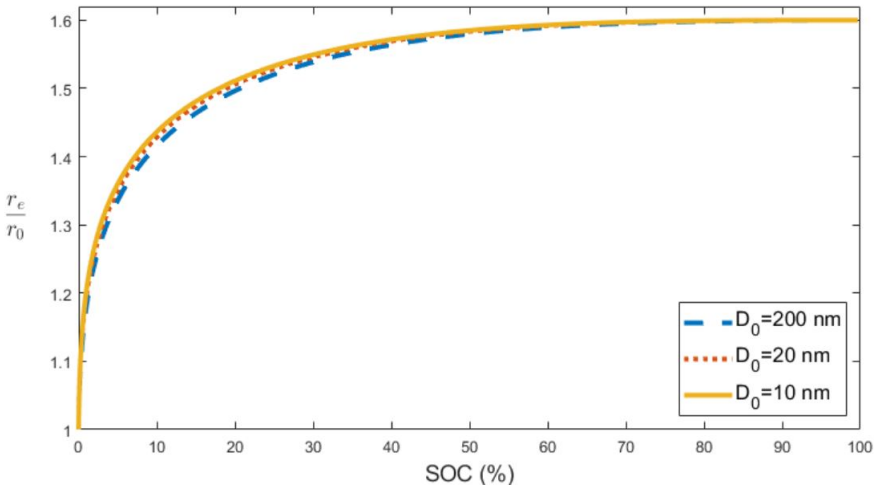

Figure 5: Effect of the particle size on the evolution of the normalized particle radius (r_e/r_0) during lithiation predicted by the elastoplastic model using the large strain approach (material data reported in Table 2).

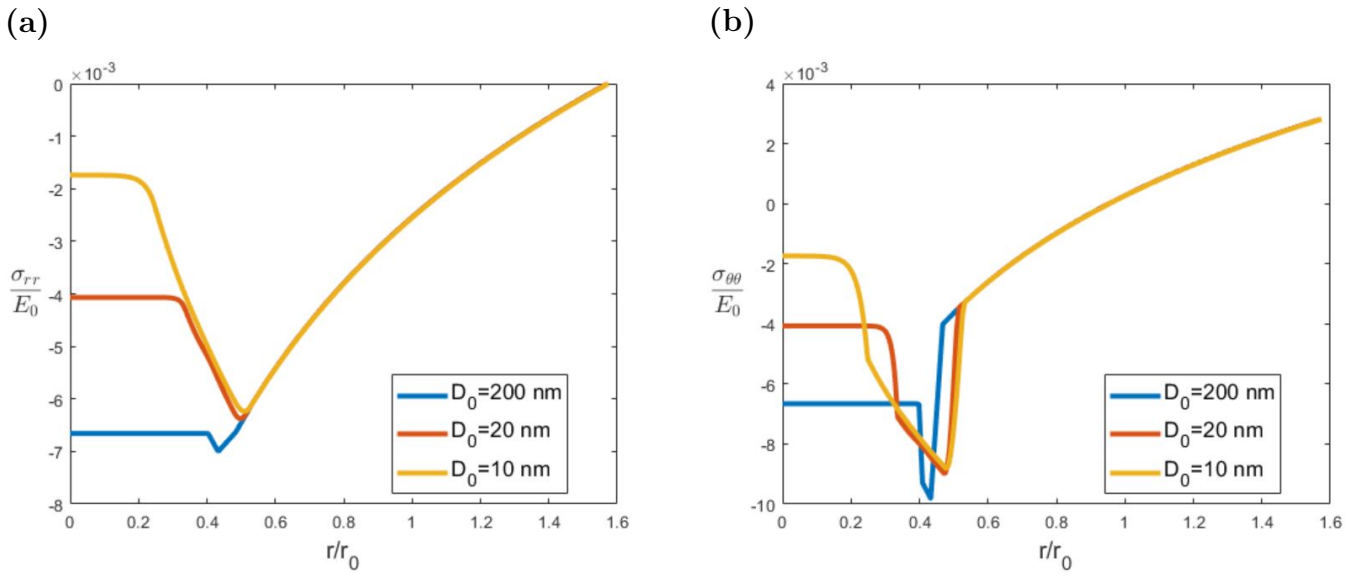

Figure 6: Effect of the particle size on the radial distribution of stresses predicted by the elastoplastic large strain approach when $SOC = 45\%$ (material data reported in Table 2). (a) radial stress (b) hoop stress.

scattering vector measured by Tardif et al. (2017) is used to compute the time evolution of the volume average of the elastic strain for different crystallographic directions of the pristine cores, as reported in Figure 7. It shows a slight variation with respect to the crystallographic direction. The particles of the electrode in the experiment are divided in two populations of different sizes: large particles (index (1), mean radius $r_{0(1)} \approx 50$ nm, initial volume fraction $x_{v(1)}$) and small particles (index (2), mean radius $r_{0(2)} \approx 17.5$ nm, initial volume fraction $x_{v(2)} = 1 - x_{v(1)}$). At a given time (t), the lithiation front positions of the large and small particles are denoted by $r_{c(1)}(t)$ and $r_{c(2)}(t)$, respectively. These positions should be considered as average values over the entire population of either large or small particles. We aim to compare the average elastic strain obtained with our lithiation model during the first

lithiation to the experimental one. This first lithiation is divided in three steps (for more details see Tardif et al. (2017)). The first one is the formation of the SEI formation (from $0 \leq t \leq t_I \approx 0.4\,10^4\,s$). At any time $t > t_I$, the specific capacity $SC(t)$ is known and allows to evaluate the initial volume fraction and the lithiation front position via the mass balance of the number of lithium atoms inserted only in the silicon. This mass balance for a system with two population of particles reads:

$$\frac{(SC(t) - SC(t_I))\ M_{Si}}{F} = \sum_{i=1}^{i=2} x_{v(i)}\ \chi_{shell} \underbrace{\left(\frac{3}{(r_{0(i)})^3} \int_0^{r_{0(i)}} \hat{c}(r,t)\, r^2\, dr \right)}_{SOC_{(i)}(\mathrm{t})} \tag{17}$$

with F the Faraday constant, $M_{Si} = 28\,\mathrm{g/mol}$ the molar mass of silicon, $\chi_{shell} = 3.2$ the stoichiometry of the lithiated alloy estimated in the experiment ($Li_{3.2}\,Si$, see Tardif et al. (2017) for more details) and SOC being the state of charge as defined in section 3. The lithiation front position $r_{c(i)}(t)$ is taken into account in the concentration function $\hat{c}(r,t)$ (equation (1)). The second and third steps of the first lithiation are respectively the lithiation of the population of small particles ($t_I < t \leq t_L$) and lithiation of the population of large particles ($t_L < t \leq t_F \approx 1.9\,10^4\,s$). Knowing that small particles are lithiated at $t_L \approx 10^4\,s$ (namely, $r_{c(2)}(t_L) = 0$) while the large ones are still in their pristine state ($r_{c(1)}(t_L) = r_{0(1)}$) we can estimate from the last relation (17) the volume fraction of small particles:

$$x_{v(2)} = \frac{(SC(t_L) - SC(t_I))\ M_{Si}}{\chi_{shell}\, F} \approx 12\% \tag{18}$$

with $SC(t_L) - SC(t_I) \approx 366\,\mathrm{mA\,h\,g^{-1}}$ being the increment of the specific capacity during the lithiation of small particles. The estimated small volume fraction of approximately 12% of the population of small particles is consistent with Tardif et al. (2017). According to Tardif et al. (2017), we focus in comparing our mechanical model only with the lithiation of large particles from $t_L \approx 10^4\,s$ to $t_F \approx 1.9\,10^4\,s$. Henceforth, for $t > t_L$, the time evolution of the position of the lithiation front in the large particles is derived from the mass balance (17) expressed with the following approximation:

$$\frac{3}{(r_{0(1)})^3} \int_0^{r_{0(1)}} \hat{c}(r,t)\, r^2\, dr \approx 1 - \left(\frac{r_{c(1)}}{r_{0(1)}} \right)^3 .$$

As the thickness of the lithiation front is much smaller than the particles radius, the effect of this approximation on the evaluation of the position of the lithiation front is less than 1%. Finally, it yields:

$$t_L \leq t \leq t_F : \quad r_{c(1)}(t) = r_{0(1)} \left(1 - \left(\left[SC(t) - SC(t_L) \right] M_{Si} / \left[F\, \chi_{shell}\, x_{v(1)} \right] \right) \right)^{1/3} . \tag{19}$$

Thanks to this last relation (19), the time evolution of the logistic function introduced above (relation (1)) is expressed as a function of the time evolution of the specific capacity. The elastic moduli of the crystalline core and the outer shell of the particles are estimated with the relations (3) and (4) using $\chi_{shell} = 3.2$. Finally, the volume average elastic strain of large particles reads:

$$\bar{\varepsilon}_m(t) =< \varepsilon_m(t) >_{(1)} \tag{20}$$

with the elastic hydrostatic deformation in the crystalline core of a particle denoted as ε_m. As discussed in the previous parts of this section, the silicon core is always submitted to an homogeneous pure hydrostatic stress state. Consequently, the average elastic deformation within the silicon core of a particle is independent of its radial coordinates.

Inline with the previous discussion about the variation of the yield stress value in the lithiated shell found in the literature (section 2.2.1), two different values are considered in our analysis (0.45 GPa and 1.5 GPa), as shown in Figure 7(a), in order to evaluate its effect on the silicon core strain during lithiation. In addition, in order to take into account the small tensile strain of 0.8×10^{-4} at $t = t_L$ explained by the formation of the thin, highly lithiated, amorphous layer around the silicon nanoparticle and the SEI formation (Tardif et al. (2017)), we impose a small tension at the outer boundary of the large particles ($\approx 22\,\mathrm{MPa}$). In Figure 7(a), the evolution of the average of the elastic strain for the large particles simulated by our model is compared to experimental data. We observe that they are in good agreement as the strain in the silicon core is in tension in the beginning of lithiation and then changes for compression at around $1.3 \times 10^4\,\mathrm{s}$. We observe that our calculations best match experimental data for $\sigma_Y = 0.45\,\mathrm{GPa}$ (for that reason we have adopted this value in the previous sections). At the end of the first lithiation, the volume fraction of silicon that remains in the pristine state is approximately 68%, which is consistent with the evolution of the diffracted intensity in Tardif et al. (2017). The final lithiation front position is $r_{c(1)} = 0.9168\, r_{0(1)}$ and the average lithiation front speed corresponds to a very low charging rate ($\approx 0.45\ pm/s$).

In Figure 7(b), we have reported the predicted results corresponding to the small strain model for two different yield stress values in the lithiated shell (0.45 GPa and 1.5 GPa). In the range of the values considered in this work, the mean strain and the transition to tension to compression predicted by the small strain approach is delayed with respect to experimental data. In conclusion, the large strain approach turns out to better predict the evolution of the elastic strain of the crystalline core.

4. Effect of a carbon coating

As explained in the introduction, the use of coatings on the silicon particles aims to mitigate the degradation phenomena of silicon during its lithiation. One of the advantages of using coatings is their structural buffer effect, limiting the volume expansion of silicon and preserving the integrity of the electrode by avoiding damage to silicon particles (Luo et al. (2016)). In addition, they avoid the contact between the silicon with the electrolyte, preventing the excessive SEI formation during initial cycles. Last but not least, the coating improves the electrical conductivity in the electrode. We focus in this work on the core-shell coating concept. As illustrated in Figure 8, this type of structure is a silicon particle coated with a layer of carbon and is denoted as Si@C. We neglect the chemical strain of the carbon coating induced by lithiation (about 6% variation of volume).

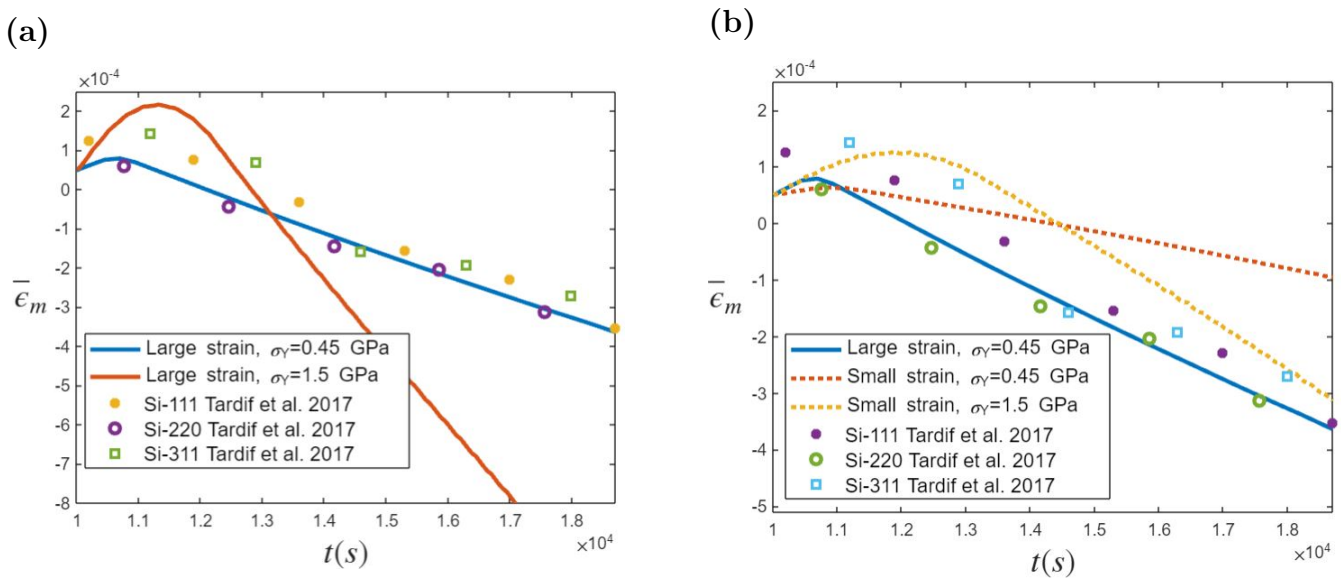

Figure 7: DRX evolution of the average elastic strain of the silicon core as a function of time (Tardif et al. (2017)) and numerical results from mechanical model (material data reported in Table 2): (a) effect of the yield stress of the lithiated silicon on the average elastic strain of the silicon core predicted by the elastoplastic large strain model. (b) Comparison of the evolution of the average elastic strain of the silicon core for small strain and large strain approaches.

4.1. Closed-form expression and semi-analytical model of the maximal stresses experienced by the carbon coating at the end of lithiation

The carbon coating is modeled as a purely elastic and isotropic material whose volume expansion due to lithiation is neglected. As the considered problem still respects the spherical symmetry, the mechanical interaction between the particle and the coating reduces to the continuity of radial stress (pressure at the interface) and displacement. Thus, the radial displacement and the three components of the stress in the coating are given by the classical solution of an elastic spherical shell submitted to an internal pressure in Appendix B. From the relation (B.2) reported in this appendix, we can express the internal pressure $P_c(t)$ as a function of the displacement of the internal radius of the coating, $u_c(r_0, t)$, namely:

$$P_c(t) = 3\,K_c \left(\frac{u_c(r_0,t)}{r_0} \right) \quad \text{with} \quad K_c = \kappa_c \left(\frac{(r_{c0}^3 - r_0^3)}{r_0^3 + \left(\frac{3\,\kappa_c\, r_{c0}^3}{4\mu_c} \right)} \right) \tag{21}$$

with κ_c and μ_c the elastic properties of the carbon coating, e_0 the thickness of the coating and r_{c0} the total initial radius of the composite particle. The constant K_c is the apparent compressibility of the coating. It depends on its elastic compressibility κ_c, the ratio κ_c/μ_c (which itself depends on its Poisson ratio) and on the ratio of its radius to its thickness. An important result for the composite particle is that the stress at the end of lithiation (t_e) is constant for a given r_0/e_0 ratio. From equations (21) and (A.13) written at the end of lithiation ($t = t_e$) and at the periphery of the silicon particle ($r = r_0$), we show that the pressure at the interface increases linearly with the chemical strain ε^c. The proportionality coefficient depends only on the apparent compressibility of the carbon coating (K_c, see relation (21))

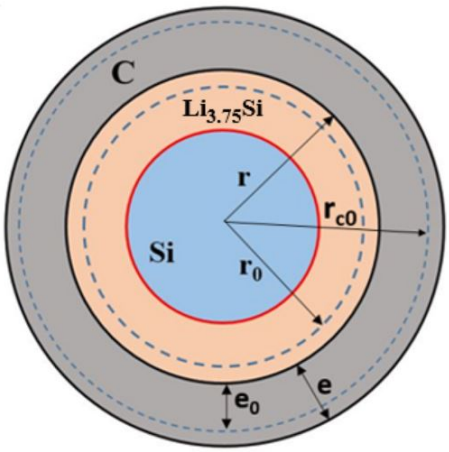

Figure 8: Composite particle with three domains and two interfaces (lithiation front in red, $Li_{3.75}Si/C$ interface in black, pure silicon in blue, $Li_{3.75}Si$ alloy in orange and carbon in gray).

and the elastic compressibility of the lithiated silicon (κ_s). It is written as:

$$P_c(t_e) = \left(\frac{3\,K_c}{1+\frac{K_c}{\kappa_s}} \right) \varepsilon^c \tag{22}$$

The maximum hoop stress in the carbon coating, at the interface of the composite particle and at the end of the lithiation, is written using equations (22) and (B.1):

$$\sigma_{\theta\theta}^{c/max}(t_e) = 0.5\ P_c(t_e)\ \frac{2\left(\frac{r_0}{e_0}\right)^3 + \left(1+\frac{r_0}{e_0}\right)^3}{\left(1+\frac{r_0}{e_0}\right)^3 - \left(\frac{r_0}{e_0}\right)^3} \tag{23}$$

Remarkably, the maximum hoop stress experienced by the coating depends only on the elastic properties of the fully lithiated silicon particle and the coating, the chemical strain induced by lithiation as well as the ratio between the radius of the particle and the thickness of the coating. Injecting the expression of the pressure at the interface (22) in the last relation, the maximum hoop stress reads finally:

$$\sigma_{\theta\theta}^{c/max}(t_e) = \left(\frac{3\,K_c}{1+\frac{K_c}{\kappa_s}} \right) \left(\frac{\left(\frac{r_0}{e_0}\right)^3 + \frac{1}{2}\left(1+\frac{r_0}{e_0}\right)^3}{\left(1+\frac{r_0}{e_0}\right)^3 - \left(\frac{r_0}{e_0}\right)^3} \right) \varepsilon^c \tag{24}$$

This closed-form expression remains an approximation as the large displacements have been neglected until now. As the dilatation of the particle increases when the apparent rigidity of the coating decreases, the estimation (24) should deviate from finite element calculations when, for instance, the ratio between the particle radius and the coating thickness increases. In order to take into account the geometry variation in the solution, the previous equations are written in the infinitesimal form, considering the current radius/coating thickness denoted by r and e respectively. For a given increment of the chemical strain, $\delta\varepsilon^c$, the

variations of the geometrical parameters are solution of the following system of differential equations (more details are given in the Appendix D):

$$\begin{aligned} \delta\hat{r} &= \frac{\delta\varepsilon^c\,\hat{r}}{1+\frac{\hat{K}_c}{\kappa_s}} \\ \delta\hat{e} &= \frac{3\,\hat{K}_c\;\delta\varepsilon^c\,\hat{f}}{1+\frac{\hat{K}_c}{\kappa_s}} \end{aligned} \tag{25}$$

with $\hat{r} = r/r_0$ and $\hat{e} = e/e_0$ the adimensional geometry variables and:

$$\hat{K}_c(e_0/r_0,\hat{r},\hat{e}) = \kappa_c\,\frac{\left(\hat{r}+\hat{e}\left(\frac{e_0}{r_0}\right)\right)^3-\hat{r}^3}{\hat{r}^3+\frac{3\,\kappa_c\left(\hat{r}+\hat{e}\left(\frac{e_0}{r_0}\right)\right)^3}{4\mu_c}} \tag{26}$$

$$\hat{f}(e_0/r_0,\hat{r},\hat{e}) = \frac{\hat{r}^3\,\hat{e}-\left(\left[\hat{r}+\hat{e}\left(\frac{e_0}{r_0}\right)\right]^2-\hat{r}^2\right)\left(\hat{e}+\left(\frac{r_0}{e_0}\right)\hat{r}\right)\hat{r}}{\left(\hat{r}+\hat{e}\left(\frac{e_0}{r_0}\right)\right)^3-\hat{r}^3}.$$

As explained in the Appendix D, the final value of the chemical strain must be chosen so as to find the experimental results in the particular case of a free particle (no coating). For each r_0/e_0 value, we solve the system of equations (25) in order to obtain the updated geometry ($\hat{e}$ and $\hat{r}$). From this, we can deduce the interface pressure and hoop stress from equations (22) and (23) by substituting in these equations the initial particle geometry (r_0, e_0) by the updated ones. To assess the relevance of this original semi-analytical solution, its predictions are compared on Figure 9 to the ones derived from the finite-element model described previously. On this Figure are compared the particle dimensions, the pressure at the interface and the maximal hoop stress in the coating at the end of lithiation with respect to the ratio of the initial particle diameter over the coating thickness, D_0/e_0. Finite element and semi-analytical predictions are very close regardless of the elastic moduli of the lithiated particle and the coating. For that reason the semi-analytical model will be used in the following sections to estimate the stresses in the coating and study its fracture properties.

4.2. Interpretation of the experimental data provided by Li et al. (2016), fracture analysis of the carbon coating

The lithiation experiment of carbon-coated silicon particles reported in Li et al. (2016) was carried out on several particles sizes of crystalline silicon ($D_0 = 10$ nm to 150 nm) with coating of amorphous carbon ($e_0 = 6$ nm to 12 nm). As explained in the introduction, the fact that all the coated particles break for a diameter of the silicon core upper than $D_0 = 70$ nm whatever the thickness e_0 of the coating, is explained by the apparition of radial cracks in the carbon coating during the lithiation of the particles. On the next Figure 10(a), we have reported the maximal opening (hoop) stress in the coating as a function of the geometrical ratio D_0/e_0. As remarked by Li et al. (2016), the experimental results (in terms of fracture / non fracture) are well ordered, the fuzzy zone in the range $D_0/e_0 = [3.5;\ 7]$ can be

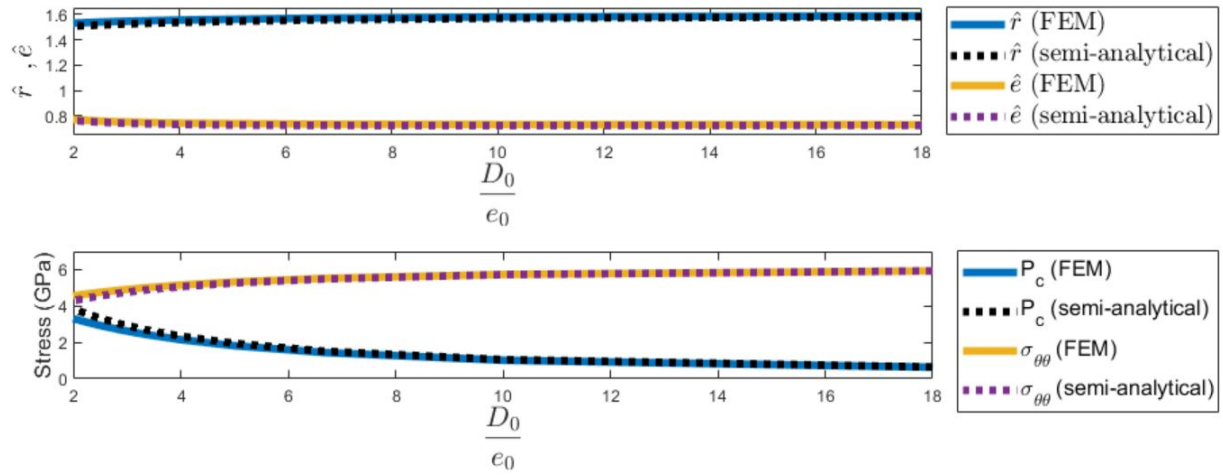

Figure 9: Particle dimensions (internal normalized radius $\hat{r}$ and normalized thickness $\hat{e}$ of the coating), internal pressure P_c and maximum hoop stress $\sigma_{\theta\theta}$ in the coating at the end of lithiation. Predictions of the finite element large strain model are compared to the ones of the semi-analytical model with updated geometry ($E_C = 10$ GPa, $E_S = 40$ GPa and other material data reported in Table 2).

interpreted as the scatter of the carbon strength (estimated by these authors between 6 and 12 GPa). As the results reported in Li et al. (2016) have been obtained with a two-dimensional elastoplastic model (circular section with plane strain assumption, see the supplementary information attached to this contribution), they are not quantitatively comparable to our results reported in Figure 10(a) (in consequence they are not shown in this figure).

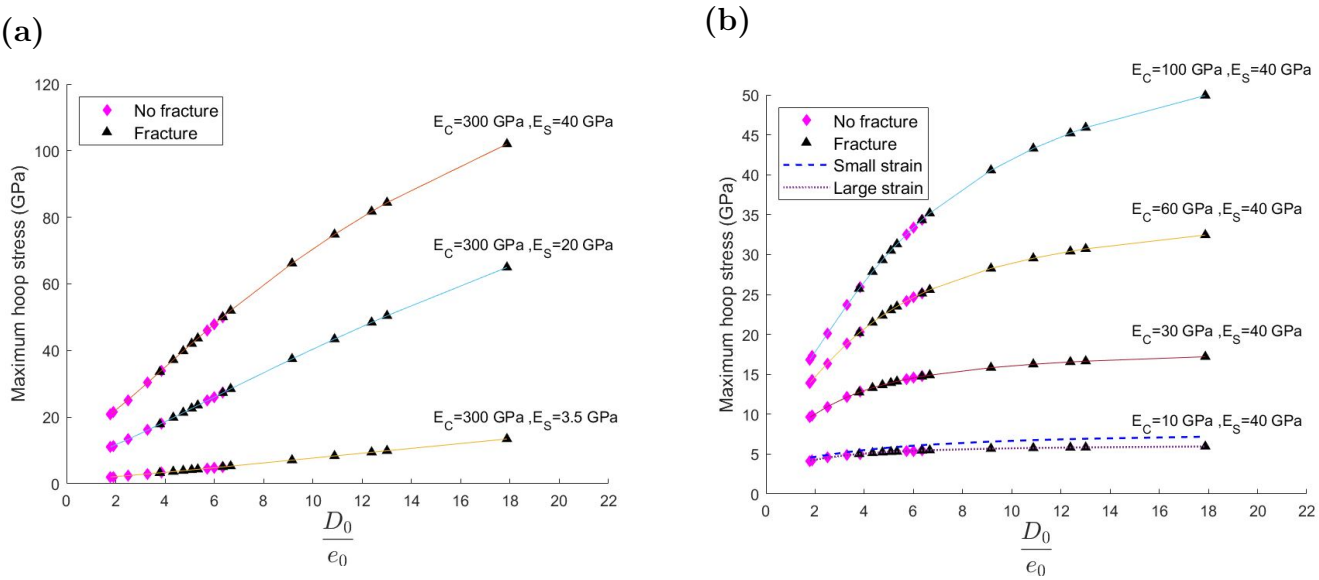

Figure 10: Maximum hoop stress in the coating with respect to D_0/e_0 predicted by the semi-analytical with updated geometry model at the end of the lithiation ($\nu_s = 0.22$ and $\nu_C = 0.25$ (Li et al. (2016))) : (a) Maximum hoop stress for different values of the Young modulus of the lithiated silicon (for fixed $E_C = 300$ GPa). (b) Maximum hoop stress for different values of the Young modulus of the carbon coating (for fixed $E_S = 40$ GPa) and comparison with small strain closed-form solution model for $E_C = 10$ GPa.

As predicted by the closed-form expression (24), the elastic properties of the lithiated

silicon and the coating drive the maximal hoop stress experienced in the coating. However, the values of these Young moduli adopted by Li et al. (2016) remain questionable. First, the Young modulus of the lithiated silicon for which the experimental results from Kushima et al. (2012) are not relevant as seen in section 2.2.1 and lead to an underestimation of the fracture stresses of the coating. This trend is illustrated in Figure 10(a) where the Young modulus of lithiated silicon is increased progressively from $E_S = 4$ GPa to $E_S = 40$ GPa (on this Figure, the Young modulus of the carbon coating denoted by E_C equals 300 GPa in a manner consistent with the choice proposed in Li et al. (2016)). We observe that stress increases in average 5 times for $D_0/e_0 = 3.5$ and 8 times for $D_0/e_0 = 7$ in the range of lithiated silicon Young modulus considered (from 4 GPa (Li et al. (2016)) to 40 GPa).

Second, the discussion about the young's modulus value of the carbon coating, E_C, is also of interest. It is useful at this stage to recall that the amorphous carbon was synthesized in Li et al. (2016) via pyrolysis of sucrose in a furnace at $800°C$. At this relatively low temperature, the final carbon is a pyrolytic amorphous carbon (thesis of Farbos (2014)). The Young modulus of pyrolytic carbon fabricated by chemical vapor deposition (CVD) techniques has been measured by nanoindentation in several works. Depending on the final porosity of the coating, the Young modulus ranges from 8.8 to 34.6 GPa (see Sheikholeslami et al. (2018)). These values mentioned above are far below the value $E_C = 300$ GPa used by Li et al. (2016) for their calculations. In consideration of those references, if we consider the Young modulus being in the order of a few dozens of GPa, we observe in Figure 10(b) a significant decrease of the maximum hoop stress when the Young modulus of the coating decreases (the Young modulus of the lithiated silicon being kept fixed, $E_S = 40$ GPa).

In general terms, we can observe in Figure 10 that the values of the Young moduli of the lithiated silicon and the coating do not modify the interval D_0/e_0 defining the fuzzy zone ($3.5 \leq D_0/e_0 \leq 7$). This is because the maximal opening stress remains in all cases an increasing function of the geometrical parameter D_0/e_0. It's worth remarking at this stage that decreasing the value of the Young modulus lowers considerably the sensibility of the maximum hoop stress to the geometrical coefficient D_0/e_0. Therefore we observe that the maximum hoop stress varies between 4.9 GPa for $D_0/e_0 = 3.5$ to 5.5 GPa for $D_0/e_0 = 7$. As a result, the estimation of the fracture strength of the coating is considerably tighter (the average value is 5.2 ± 0.3 GPa) compared to that estimated by Li et al. (2016) and reported above (between 6 and 12 GPa). Considering the Young moduli $(E_S, E_C) = (40, 10)$ GPa, the effect of the large strain computation remains moderate even at high D_0/e_0 ratios.

To conclude on this subject, the elastic properties of the carbon coating are intimately linked to the manufacturing process and therefore difficult to estimate *a priori*. Their measurement is therefore needed. Alternatively, it would be of great interest to have measurements of carbon-coated silicon diameters during the lithiation of particles. As the diameter of the lithiated particles strongly depends on the elastic rigidity of the coating, this type of measurement would allow to determine its value from the simulation, by an inverse method.

4.3. Mechanical behaviour of the silicon particle during lithiation

We have so far studied the mechanical state of the coating at the end of lithiation but we now wish to study the mechanical response of the particle during the entire duration of the lithiation. Since the semi-analytical model proposed in section 4.1 only calculates the final mechanical state in the coating, the next results are derived by using the elastoplastic large

strain finite-element model presented in section 2.2.3. In view of the previous discussion, the elastic properties of amorphous carbon adopted are $E_C = 10$ GPa and $\nu_C = 0.25$ (Li et al. (2016)), even if and as explained above, this value of Young's modulus remains arbitrary and constitutes a lower limit. The elastic properties of the silicon are consistent with the previous simulations: elastic properties vary as a function of the state of charge according to relations (3) and (4) while the yield stress of the lithiated silicon is the one determined by comparison with experiments in section 3.3, namely 0.45 GPa. The thickness of the lithiation front is the same as previously, namely 1 nm.

We observe in Figure 11(a) the evolution of the increasing external radius of the silicon particle during lithiation for different particle diameter to coating thickness ratio. The final external radius of the particle decreases slightly for increasing values of the thickness of the coating as well as its apparent compliance. Therefore the volume expansion of silicon is around 280% in the case of $D_0/e_0 = 5$ compared to 300% for an uncoated particle. This decrease remains small as the Young modulus of the coating is four times lower than the one of the lithiated silicon. Figure 11(b) shows that the maximum hoop stress in the carbon coating is an increasing function of the state of charge and is slightly dependent on the silicon particle size. The stress state at the end of lithiation does not depend on the size of the particles. Figure 12 shows the radial and hoop stress evolution as a function of the radius at the end of lithiation for three different ratios D_0/e_0. The coating domain is represented with dashed line and the silicon with continuous line. Obviously, the pushing out effect vanishes in the silicon particle which now is submitted to compressive hoop stresses. We also observe a jump in hoop stress at the interface between the silicon particle and the coating that changes from compression in the silicon to tension in the coating. As the outer boundary of the coating is stress free, the radial component of the stress in the particle and the coating is entirely in compression (Figure 12(b)).

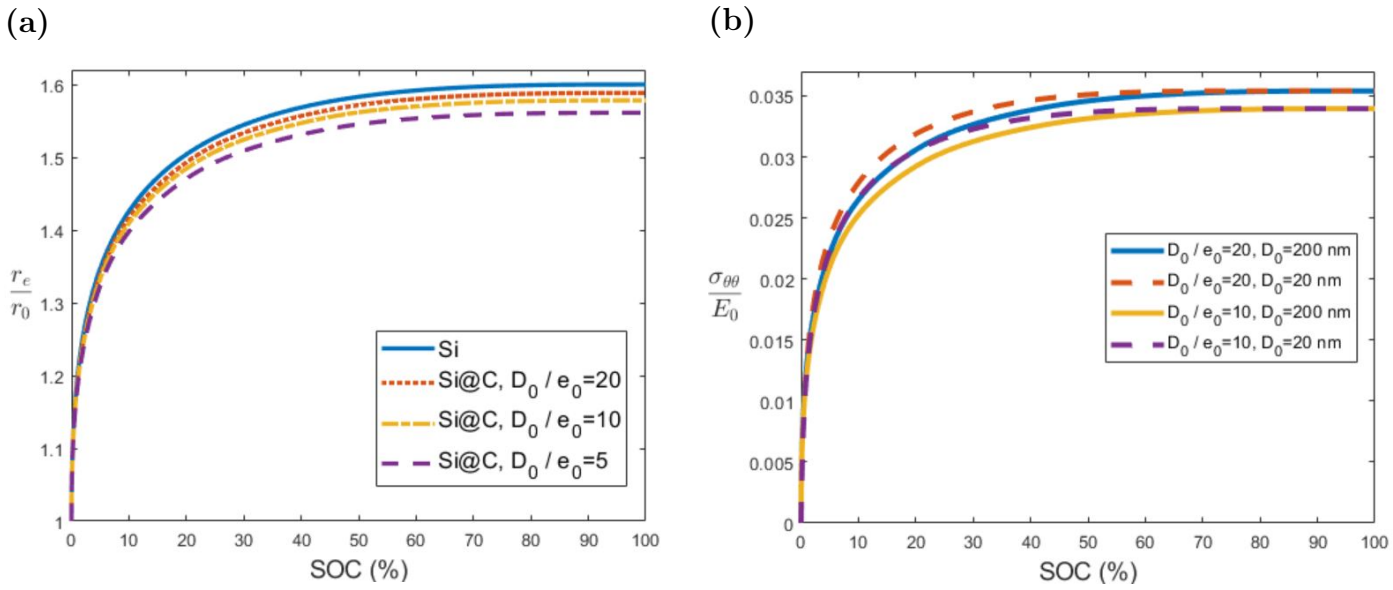

Figure 11: Effect of the coating thickness of the composite particle on (a) evolution of the external radius of the silicon particle during lithiation for different initial thicknesses e_0 of the coating (the initial diameter D_0 of the silicon particle equals 200 nm, $E_C = 10$ GPa and (b) Evolution of the maximum hoop stress in the carbon coating for two particles diameters (200 nm and 20 nm) and two coating thicknesses. Material data for silicon and lithiated silicon reported in Table 2.

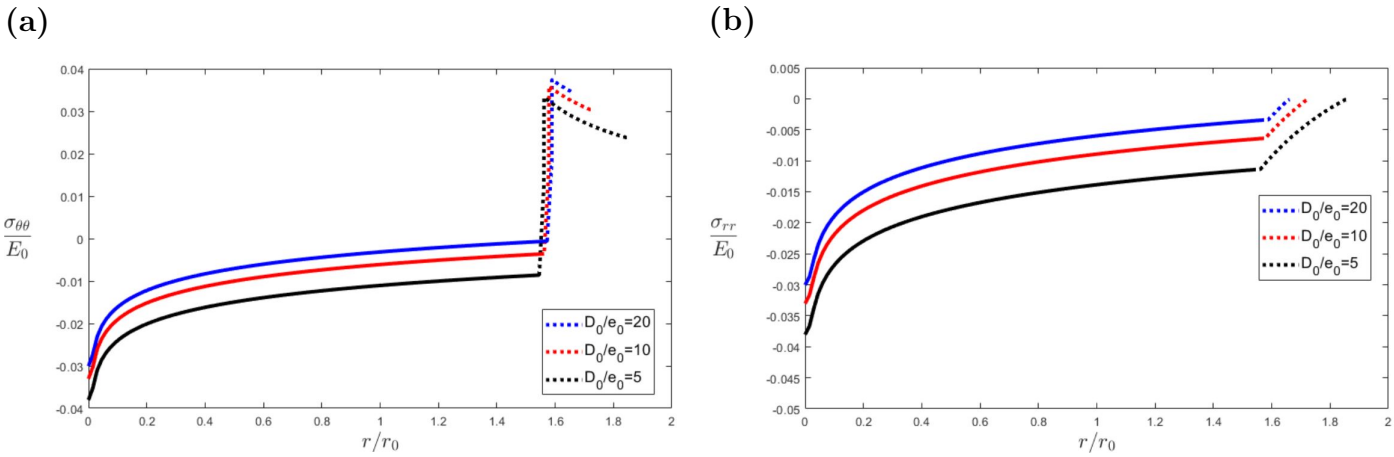

Figure 12: Stress field at the end of lithiation for a 200 nm diameter particle with $E_C = 10$ GPa (a) Normalized hoop stress ; (b) Normalized radial stress. Material data for silicon and lithiated silicon reported in Table 2.

5. Conclusions

In this work we analysed the stress and strain evolution in coated and uncoated silicon nanoparticles during their first lithiation. We developed different mechanical models taking into account the various phenomena observed experimentally during the lithiation of silicon such as phase change, material and geometrical nonlinearities. The lithium concentration in the silicon particle is given by a sigmoid function (called logistic function) to represent the sharp reaction front between phases. In addition our work presents a novel comparison between experimental data and a state-of-the-art mechanical model of the lithiation of silicon nanoparticles.

First, we proposed an original small strain semi-analytical mechanical model. The resolution of this model is reduced to a nonlinear integro-differential system, with two unknown scalar fields, solved by a finite difference method and an implicit Euler temporal integration method. Second, a large strain model was developed using a logarithmic strain framework associated to an updated lagrangian approach. We applied both models for the estimation of the stress level and strain in coated and uncoated silicon nanoparticles during their lithiation. For an uncoated nanoparticle, the results obtained are qualitatively consistent with others numerical models in the literature such as Jia and Liu (2016) and Jia and Li (2016). Moreover, we discussed the effect of the silicon particle size in the evaluation of its radius and stress, considering in the study different particle sizes and a fixed front length. We revealed that stresses in the fully lithiated particle is independent of its size. Nevertheless, in an intermediate state, the stress in the silicon pristine increases with respect to the particle size, consequently increasing the stored elastic energy and hence the risk of fracture. To our knowledge, this size effect has not been addressed in the past, at least with the state-of-the-art model adopted.

The numerical predictions were compared with measurements obtained by XRD by Tardif et al. (2017). Our large strain FEM model predicts well the evolution of the strain in the silicon crystalline core during the first lithiation of a crystalline silicon nanoparticle. The optimal value of the yield stress in the lithiated shell that better agrees with experimental data reported in Tardif et al. (2017) was also estimated. That value is consistent with the range reported in the literature. We evidenced that large strain modeling are needed to predict correctly the compressive stress evolution in the crystalline core. In the future and in order to study potential strain rate effects on the plastic flowing of the lithiated shell, it would be interesting to make similar experiments applying different lithiation speeds. This would be a way to measure a potential strain rate effect on the plastic flow of the lithiated shell but the study of higher lithiation rates may require to solve explicitly the diffusion problem and to take into account the two-way coupling between diffusion and stress.

Our model has been extended to a composite structure in order to study the coating of silicon nanoparticles. A new semi-analytical approach with updated geometry has been proposed and compares well with the full finite element model. Thanks to this model, closed-form relations of the maximal hoop stress experienced by the coating have been derived. It depends on the strain induced by lithiation, the elastic properties of the lithiated silicon and the coating as well as the ratio between the radius of the particle and the thickness of the coating. As expected, the coating limits the silicon particles expansion. In addition, the hoop stress experienced by the coating is maximal at its inner surface and at the end of the

lithiation process.

These results have been used to interpret experimental results reported in Li et al. (2016) and related to the fracture of Si@C particles during lithiation. In addition to the fact that these new interpretations model the particles as spheres, which is more realistic than the former ones in Li et al. (2016) (particles were modeled as cylinders), we were able to appreciate the effect of the large strain modeling on the predicted maximum hoop stress in the coating. We have also shown that adopting more appropriate values of the elastic moduli of the lithiated silicon and the carbon coating results in tighter bounds on the fracture strength of amorphous carbon. Nevertheless, as the chosen value for the elastic modulus of the coating remains arbitrary, having measurements of carbon-coated silicon diameters during the lithiation of particles would be of great interest to appreciate the relevance of the model.

Acknowledgements

This work was partially developed within the framework of the MISTRAL joint research laboratory between the Aix-Marseille University, the French National Research Center (CNRS), Centrale Marseille and the French Alternative Energies and Atomic Energy Commission (CEA). The authors are grateful for the financial support provided by the CEA Energy Division through the programs "Multiscale battery simulation applied to electrode materials" and Cross-cutting basic research. The authors also acknowledge S. Tardif and S. Lyonnard for their helpfull advices.

Appendix A. Derivation of relations (9) and (10) (semi-analytical solution)

For the 1D spherical problem in infinitesimal strain approach with spherical coordinates (r, θ, ϕ) and isotropic lithiation, the displacement field solution is $\boldsymbol{u}(r,t) = u(r,t)\,\boldsymbol{e_r}$ ($\boldsymbol{e_r}$ denotes the unit vector in a radial direction). Therefore, the strain field and the stress field are both diagonal. The total deformation is given as:

$$\underline{\underline{\boldsymbol{\varepsilon}}}(r,t) = \begin{pmatrix} \frac{\partial u}{\partial r}(r,t) & 0 & 0 \\ 0 & \frac{u(r,t)}{r} & 0 \\ 0 & 0 & \frac{u(r,t)}{r} \end{pmatrix} \tag{A.1}$$

with $u(0,t) = 0$. Denoting by $\underline{\underline{\boldsymbol{\sigma}}}(r,t)$ the stress tensor, the equilibrium equation and boundary conditions are:

$$\frac{\partial \sigma_{rr}}{\partial r}(r,t) + \frac{2}{r}\left(\sigma_{rr}(r,t) - \sigma_{\theta\theta}(r,t)\right) = 0 \qquad\qquad \sigma_{rr}(r_0) = -P_c(t) \tag{A.2}$$

where $P_C(t)$ is the pressure to be determined for a particle with coating and for a particle without coating it reads $P_c(t) = 0$. We define the signed equivalent stress $\sigma_S(r,t) = \sigma_{\theta\theta}(r,t) - \sigma_{rr}(r,t)$ and the Von Mises stress reads $\sigma_{eq} = |\sigma_{\theta\theta} - \sigma_{rr}|$. The deviatoric part of the stress and strain tensors, $\underline{\underline{\boldsymbol{s}}}(r,t)$ and $\underline{\underline{\boldsymbol{e}}}(r,t)$ respectively, are:

$$\begin{aligned} \underline{\underline{\boldsymbol{e}}}(r,t) &= \frac{\varepsilon_{rr}(r,t) - \varepsilon_{\theta\theta}(r,t)}{3}\,\underline{\underline{\boldsymbol{d}}} \\ \underline{\underline{\boldsymbol{s}}}(r,t) &= \frac{\sigma_{rr}(r,t) - \sigma_{\theta\theta}(r,t)}{3}\,\underline{\underline{\boldsymbol{d}}} \end{aligned} \tag{A.3}$$

with

$$\underline{\underline{\boldsymbol{d}}} = \begin{pmatrix} 2 & 0 & 0 \\ 0 & -1 & 0 \\ 0 & 0 & -1 \end{pmatrix}. \tag{A.4}$$

Derivating with respect to time the compatibility equations yields the following relation between the radial and tangential components of the strain rate:

$$\dot{\varepsilon}_{rr}(r,t) - \dot{\varepsilon}_{\theta\theta}(r,t) = \frac{r}{3}\frac{\partial}{\partial r}\left(\frac{V_r(r,t)}{r}\right) \tag{A.5}$$

with $V_r(r,t) = \dot{u}(r,t)$. The deviatoric part of the equation (8) is written as:

$$\left(\dot{\varepsilon}_{rr}(r,t) - \dot{\varepsilon}_{\theta\theta}(r,t)\right)\underline{\underline{\boldsymbol{d}}} = -\left(\frac{\dot{\sigma}_S(r,t)}{2\mu(r,t)} - \frac{\sigma_S(r,t)\dot{\mu}(r,t)}{2\mu^2(r,t)}\right)\underline{\underline{\boldsymbol{d}}} - 3\,\sigma_S(r,t)\frac{\partial w}{\partial \widetilde{\sigma}}\,\underline{\underline{\boldsymbol{d}}}. \tag{A.6}$$

Injecting (A.5) in this last relation yields:

$$\dot{\sigma}_S(r,t) + \sigma_S(r,t)\left(6\mu(r,t)\,\frac{\partial w}{\partial \widetilde{\sigma}}(r,\widetilde{\sigma}) - \frac{\dot{\mu}(r,t)}{\mu(r,t)}\right) = -2\mu(r,t)\left(r\frac{\partial}{\partial r}\left(\frac{V_r(r,t)}{r}\right)\right). \tag{A.7}$$

From the hydrostatic part of the equation (8), we obtain:

$$\varepsilon_m(r,t) = \frac{1}{3\kappa}\sigma_m(r,t) + \varepsilon^c(r,t) \tag{A.8}$$

where the mean strain $\varepsilon_m = (\varepsilon_{rr} + 2\varepsilon_{\theta\theta})/3$ can be expressed as a function of the radial displacement, namely:

$$\varepsilon_m(r,t) = \frac{1}{3\,r^2}\frac{\partial}{\partial r}\left(r^2\,u(r,t)\right). \tag{A.9}$$

Likewise, the equilibrium equation allows to express the hydrostatic stress $\sigma_m = (\sigma_{rr}+2\sigma_{\theta\theta})/3$ as a function of the radial component:

$$\sigma_m(r,t) = \frac{1}{3\,r^2}\,\frac{\partial}{\partial r}\Big(r^3\,\sigma_{rr}(r,t)\Big). \tag{A.10}$$

Injecting relations (A.9) and (A.10) in (A.8) gives the following expression of the radial stress:

$$r^3\sigma_{rr}(r,t) = 3\int_0^r \kappa(x,t)\,\frac{\partial}{\partial x}\left[x^2u(x,t)\right]\,dx - 9\int_0^r \kappa(x,t)\,\varepsilon^c(x,t)\,x^2\,dx. \tag{A.11}$$

The integration by parts of the first term of the right-hand side of the previous equation yields:

$$\int_0^r \kappa(x,t)\,\frac{\partial}{\partial x}\left[x^2u(x,t)\right]\,dx = \kappa(r,t)\,r^2u(r,t) - \int_0^r \frac{\partial}{\partial x}\left[\kappa(x,t)\right]x^2u(x,t)\,dx. \tag{A.12}$$

So that, the final expression of the radial stress reads:

$$\sigma_{rr}(r,t) = 3\kappa(r,t)\,\frac{u(r,t)}{r} - \frac{3}{r^3}\int_0^r \frac{\partial}{\partial x}\left[\kappa(x,t)\right]x^2u(x,t)\,dx - \frac{9}{r^3}\int_0^r \kappa(x,t)\,\varepsilon^c(x,t)\,x^2\,dx. \tag{A.13}$$

Applying the equilibrium equation, we obtain the following relation between σ_S and the radial stress:

$$\sigma_S(r,t) = \frac{r}{2}\frac{\partial\sigma_{rr}}{\partial r}(r,t). \tag{A.14}$$

Using relations (A.7, A.13, A.14), we obtain a system of nonlinear equations (9,10) whose variables are $\sigma_S(r,t)$ and $u(r,t)$ and whose initial conditions are zero.

Appendix B. Elastic solution for carbon coating submitted to an internal pressure

During the expansion of a silicon particle of initial radius r_0, the carbon coating is submitted to the internal pressure $P_c(t)$. The solution for carbon coating is computed using the problem of a spherical shell of external radius r_{c0} submitted to an internal pressure:

$$\underline{\underline{\boldsymbol{\sigma}}}^c(r,t) = \frac{P_c(t)}{1-\left(\frac{r_0}{r_{c0}}\right)^3}\left(\frac{r_0}{r_{c0}}\right)^3\underline{\underline{\boldsymbol{I}}} - \frac{0.5P_c(t)}{1-\left(\frac{r_0}{r_{c0}}\right)^3}\left(\frac{r_0}{r}\right)^3\underline{\underline{\boldsymbol{d}}}. \tag{B.1}$$

The displacement reads:

$$u_c(r,t) = \frac{P_c(t)\,r\,r_0^3}{3\kappa_c\left({r_{c0}}^3 - r_0^3\right)} + \frac{P_c(t)\,r_{c0}^3}{4\mu_c\left({r_{c0}}^3 - r_0^3\right)}\left(\frac{r_0^3}{r^2}\right) \tag{B.2}$$

with κ_c and μ_c the elastic properties of the coating. At the interface with silicon, conditions of continuity are $\sigma_{rr}^c(r_0,t) = \sigma_{rr}(r_0,t) = -P_c(t)$ and $u(r_0,t) = u_c(r_0,t)$.

Appendix C. Finite difference method (semi-analytical solution)

In order to solve the system of equations (9) and (10) numerically, we discretize the spatial domain in N points with $i = 1, 2...N$, with $0 < r_1, r_2 ... r_N = r_0$ because $u(0,t) = 0$ and $\sigma_S(0,t) = 0$. We discretize the time in M steps with $k = 1, 2, ... M$. We use the notation $\hat{\sigma}_i^k = \hat{\sigma}(r_i, t_k)$ and $\hat{u}_i^k = \hat{u}(r_i, t_k)$. We use the trapezoidal rule for the calculation of integrals. We consider the general case of a sphere with a pure elastic carbon coating. The discretized equation (10) gives in the case of free outer boundary condition:

$$\hat{\sigma}_i^k = \frac{3r_i}{2}\,\hat{\kappa}(r_i,t_k)\left(\frac{\hat{u}_{i+1}^k - \hat{u}_i^k}{\Delta r}\right) + \frac{9}{2r_i^3}\int_0^{r_i}\frac{\partial\hat{\kappa}}{\partial x}(x,t)\,x^3\hat{u}(x,t)\,dx + G(r_i,t_k),\ 1 \le i \le N-1$$

$$\hat{\sigma}_N^k = \frac{3r_0}{2}\,\hat{\kappa}(r_0,t_k)\left(\frac{\hat{u}_N^k - \hat{u}_{N-1}^k}{\Delta r}\right) + \frac{9}{2}\,\hat{\kappa}(r_0,t_k)\hat{u}_N^k + \frac{3}{2}\,\hat{p} - \frac{9}{2r_0^2}\frac{\partial\hat{F}}{\partial r}(r_0,t_k),\ i = N \tag{C.1}$$

with

$$\hat{G}(r_i,t_k) = \frac{27}{2r_i^3}\,\hat{F}(r_i,t_k) - \frac{9}{2r_i^2}\frac{\partial\hat{F}}{\partial r}(r_i,t_k) \tag{C.2}$$

and $\hat{p} = P_c(t)/\sigma_Y$ is the contribution from the normalized pressure at the interface between the silicon and the pure elastic carbon coating given as:

$$\hat{p} = \hat{K_c}\,\hat{u}_N^k. \tag{C.3}$$

with $\hat{K_c} = K_c/\sigma_Y$. The equation (C.1) in matrix form is:

$$\hat{\boldsymbol{\sigma}}^k = \underline{\underline{\boldsymbol{A}}}^k\,\hat{\boldsymbol{u}}^k + \hat{\boldsymbol{G}}^k \tag{C.4}$$

with $\hat{\boldsymbol{u}}^k = (\hat{u}_1^k ... \hat{u}_N^k)^T$ and $\hat{\boldsymbol{\sigma}}^k = (\hat{\sigma}_1^k ... \hat{\sigma}_N^k)^T$. The discretized equation (9) gives:

$$\frac{1}{\hat{\mu}(r_i,t_k)}\frac{\partial\hat{\sigma}_i}{\partial t} - \frac{\dot{\hat{\mu}}(r_i,t_k)}{\hat{\mu}^2(r_i,t_k)}\hat{\sigma}_i + 3\,\dot{\varepsilon}_0\left(\hat{\sigma}_i^2\right)^{\frac{\frac{1}{m}-1}{2}}\hat{\sigma}_i + 2r_i\,\frac{\partial}{\partial t}\left(\frac{\hat{u}_{i+1} - \hat{u}_i}{\Delta r}\right) = 0,\ 1 \le i \le N-1$$

$$\frac{1}{\hat{\mu}(r_0,t_k)}\frac{\partial\hat{\sigma}_N}{\partial t} - \frac{\dot{\hat{\mu}}(r_0,t_k)}{\hat{\mu}^2(r_0,t_k)}\hat{\sigma}_N + 3\,\dot{\varepsilon}_0\left(\hat{\sigma}_N^2\right)^{\frac{\frac{1}{m}-1}{2}}\hat{\sigma}_N + 2r_0\,\frac{\partial}{\partial t}\left(\frac{\hat{u}_N - \hat{u}_{N-1}}{\Delta r}\right) = 0,\ i = N. \tag{C.5}$$

In matrix form, the preceding equation is written as:

$$\underline{\underline{\boldsymbol{M}}}^k\,\frac{\partial\hat{\boldsymbol{\sigma}}}{\partial t} + \underline{\underline{\boldsymbol{P}}}^k\,\hat{\boldsymbol{\sigma}}^k + \boldsymbol{\mathcal{F}}\left(\hat{\boldsymbol{\sigma}}^k\right) + \underline{\underline{\boldsymbol{B}}}\,\frac{\partial\hat{\boldsymbol{u}}}{\partial t} = \boldsymbol{0} \tag{C.6}$$

where $\boldsymbol{\mathcal{F}}$ is a nonlinear function of the vector $\hat{\boldsymbol{\sigma}}^k$, with the component i given by:

$$\mathcal{F}_i = 3\,\dot{\varepsilon}_0\left(\hat{\sigma}_i^2\right)^{\frac{\frac{1}{m}-1}{2}}\hat{\sigma}_i. \tag{C.7}$$

We use an implicit temporal scheme in the equation (C.6), which yields:

$$\underline{\underline{\boldsymbol{M}}}^{k+1}\left(\frac{\hat{\boldsymbol{\sigma}}^{k+1}-\hat{\boldsymbol{\sigma}}^{k}}{\Delta t}\right)+\underline{\underline{\boldsymbol{P}}}^{k+1}\,\hat{\boldsymbol{\sigma}}^{k+1}+\boldsymbol{\mathcal{F}}\left(\hat{\boldsymbol{\sigma}}^{k+1}\right)+\underline{\underline{\boldsymbol{B}}}\left(\frac{\hat{\boldsymbol{u}}^{k+1}-\hat{\boldsymbol{u}}^{k}}{\Delta t}\right)=\mathbf{0}. \tag{C.8}$$

We note $\hat{\boldsymbol{\varphi}}^{k}=\left(\hat{\boldsymbol{\sigma}}^{k}\ \hat{\boldsymbol{u}}^{k}\right)^{T}$ and rearrange the equations (C.4) and (C.8) to obtain:

$$\underline{\underline{\boldsymbol{H}}}^{k+1}\hat{\boldsymbol{\varphi}}^{k+1}+\boldsymbol{\mathcal{G}}\left(\hat{\boldsymbol{\varphi}}^{k+1}\right)+\boldsymbol{\mathcal{J}}\left(\hat{\boldsymbol{\varphi}}^{k}\right)=\mathbf{0} \tag{C.9}$$

with

$$\underline{\underline{\boldsymbol{H}}}^{k+1}=\begin{pmatrix}\frac{1}{\Delta t}\underline{\underline{\boldsymbol{M}}}^{k+1}+\underline{\underline{\boldsymbol{P}}}^{k+1} & \frac{1}{\Delta t}\underline{\underline{\boldsymbol{B}}}\\ \underline{\underline{\boldsymbol{I}}} & -\underline{\underline{\boldsymbol{A}}}^{k+1}\end{pmatrix} \tag{C.10}$$

$$\boldsymbol{\mathcal{J}}\left(\hat{\boldsymbol{\varphi}}^{k}\right)=\begin{pmatrix}-\underline{\underline{\boldsymbol{M}}}^{k+1}\hat{\boldsymbol{\sigma}}^{k}\,\frac{1}{\Delta t}-\underline{\underline{\boldsymbol{B}}}\,\hat{\boldsymbol{u}}^{k}\,\frac{1}{\Delta t}\\ -\hat{\boldsymbol{G}}^{k}\end{pmatrix} \tag{C.11}$$

$$\boldsymbol{\mathcal{G}}\left(\hat{\boldsymbol{\varphi}}^{k+1}\right)=\begin{pmatrix}\boldsymbol{\mathcal{F}}\left(\hat{\boldsymbol{\sigma}}^{k+1}\right)\\ \mathbf{0}\end{pmatrix}. \tag{C.12}$$

The initial condition for the iterative method of the equation (C.9) is $\hat{\boldsymbol{\varphi}}^{0}=\mathbf{0}$. After computing $\sigma_S(r,t)$, we use the equilibrium equation to calculate σ_{rr}:

$$\frac{\partial\sigma_{rr}}{\partial r}(r,t)+\frac{2}{r}\left(\sigma_{rr}(r,t)-\sigma_{\theta\theta}(r,t)\right)=\frac{\partial\sigma_{rr}}{\partial r}(r,t)-\frac{2\sigma_s(r,t)}{r}=0. \tag{C.13}$$

The radial stress σ_{rr} is written as:

$$\sigma_{rr}(r,t)=2\int_{r_1}^{r}\frac{\sigma_S(x,t)}{x}\,dx+h(t) \tag{C.14}$$

with $h(t)$ a temporal function from the boundary condition $\sigma_{rr}(r_0,t)=-P_c(t)$ given by:

$$h(t)=-P_c(t)-2\int_{r_1}^{r_0}\frac{\sigma_S(x,t)}{x}\,dx. \tag{C.15}$$

Appendix D. Derivation of equation (25)(geometry update of the coated particle at the end of lithiation)

In the model proposed in section 4.1 for the coated particle (equations (21)-(24)) the complete lithiation state of the particle is taken into account only through the compressibility modulus κ_s and the swelling ε^c. We assume hereafter that the same mechanical state is obtained by considering another loading path for the coated particle (composite sphere): at the initial time ($t=0$), the particle is lithiated in the whole domain such that the compressibility modulus is κ_s but without any swelling $\varepsilon^c(t=0)=0$; then the swelling increases until it reaches the final value ε^c which is obtained physically at the end of the lithiation. This loading can be applied incrementally and for each swelling increment $\delta\varepsilon^c$

the problem to be solve is exactly the one presented in section 4.1 (equation (25)). This approach allows to update the geometry of the coated particle (external radius of the particle and thickness of the coating) at each swelling increment. We consider a coated particle with initial geometry characterized by the radius r_0 and the thickness e_0. For a given geometry, characterized by the couple $(r,\, e)$, the apparent compressibility of the coating is given by equation (21):

$$K_c = \kappa_c \left(\frac{(r+e)^3 - r^3}{r^3 + \frac{3\kappa_c}{4\mu_c}(r+e)^3} \right)$$

or equivalently by equation (26) when using adimensional geometry variables $\hat{r} = r/r_0$ and $\hat{e} = e/e_0$. When a swelling increment $\delta\,\varepsilon^c$ is applied, the corresponding increment of the pressure δP_c is obtained by substituting in (22) the final pressure and swelling $P_c(t_e)$ and ε^c by their increments, namely:

$$\delta P_c = \delta\varepsilon^c \, \frac{3K_c}{1 + K_c/\kappa_s}$$

In the same way, substituting in $(21)_1$ $P_c(t)$ by the pressure increment δP_c, the initial external radius r_0 by its updated value r and the displacement $u_c(r_0, t)$ by the variation of the radius δr yields:

$$\delta P_c = 3\, K_c \left(\frac{\delta r}{r} \right) \tag{D.1}$$

Combining the two former relations, we obtain an expression for the infinitesimal adimensional radius variation:

$$\delta\hat{r} = \frac{\delta\varepsilon^c\, \hat{r}}{1 + \frac{\hat{K_c}}{\kappa_s}} \tag{D.2}$$

By making similar substitutions in equation (B.2) and then combining the resulting expression with (D.1), we obtain the infinitesimal variation of the coating thickness as:

$$\delta\hat{e} = \frac{3\,\hat{K}_c\; \delta\varepsilon^c\, \hat{f}}{1 + \frac{\hat{K}_c}{\kappa_s}} \tag{D.3}$$

with $\hat{K}_c$ and $\hat{f}$ given in equation (26). In the case of a free particle expansion, equation (D.2) reduces to $\delta\hat{r} = \delta\varepsilon^c\, \hat{r}$, which gives $log(\hat{r}) = \varepsilon^c$. From this analysis arises the need of a definition of the chemical expansion coefficient consistent with the experimental data. In order to meet the final volume of the particle according to experimental observations, one might use $\varepsilon^c = log(1+\beta)$ in the semi-analytical simulations with geometry update, $\beta = 0.6$ being the small strain estimate of this coefficient, see relation (2).

References

Ahmed Al-Obeidi, Dominik Kramer, Carl Thompson, and Reiner Mönig. Mechanical stresses and morphology evolution in germanium thin film electrodes during lithiation and delithiation. Journal of Power Sources, 297:472–480, 2015.

Lucas Berla, Seok Woo Lee, Yi Cui, and William Nix. Mechanical behavior of electrochemically lithiated silicon. Journal of Power Sources, 273:41–51, 2015.

Allan F Bower, Pradeep R Guduru, and Vijay A Sethuraman. A finite strain model of stress, diffusion, plastic flow, and electrochemical reactions in a lithium-ion half-cell. Journal of the Mechanics and Physics of Solids, 59(4):804–828, 2011.

Candace Chan, Hailin Peng, Gao Liu, Kevin McIlwrath, Xai Feng Zhang, Robert Huggins, and Yi Cui. High-performance lithium battery anodes using silicon nanowires. Nature Nanotechnology, 3:31–35, 2008.

Yong Seok Choi, Matt Pharr, Kyu Hwan Oh, and Joost Vlassak. A simple technique for measuring the fracture energy of lithiated thin-film silicon electrodes at various lithium concentrations. Journal of Power Sources, 294:159–166, 2015.

Michael Chon, Vijay Sethuraman, Anthony McCormick, Venkat Srinivasan, and Pradeep Guduru. Real-time measurement of stress and damage evolution during initial lithiation of crystalline silicon. Physical review letters, 107(4):045503, 2011.

Francisco Javier Quintero Cortes, Matthew Boebinger, Michael Xu, Andrew Ulvestad, and Matthew McDowell. Operando synchrotron measurement of strain evolution in individual alloying anode particles within lithium batteries. ACS Energy Letters, 3(2):349–355, 2018.

Zhiwei Cui, Feng Gao, Zhihua Cui, and Jianmin Qu. A second nearest-neighbor embedded atom method interatomic potential for li–si alloys. Journal of Power Sources, 207:150–159, 2012.

Baptiste Farbos. Structure et propriétés de carbones anisotropes par une approche couplant analyse d'image et simulation atomistique. PhD thesis, Université de Bordeaux, 2014.

Edwin Garcıa, Yet-Ming Chiang, W Craig Carter, Pimpa Limthongkul, and Catherine M Bishop. Microstructural modeling and design of rechargeable lithium-ion batteries. Journal of The Electrochemical Society, 152(1):A255, 2004.

Jiamei Guo and Zheng Jia. Stress evolution during the two-step charging of high-capacity electrode materials. Journal of Power Sources, 486:229371, 2021.

Thomas Helfer. Extension of monodimensional fuel performance codes to finite strain analysis using a lagrangian logarithmic strain framework. Nuclear Engineering and Design, 288: 75–81, 2015.

Thomas Helfer, Jeremy Bleyer, Tero Frondelius, Ivan Yashchuk, Thomas Nagel, and Dmitri Naumov. The mfront generic interface support project. Journal of Open Source Software, 5(48):2003, 2020.

Benjamin Hertzberg, Jim Benson, and Gleb Yushin. Ex-situ depth-sensing indentation measurements of electrochemically produced si–li alloy films. Electrochemistry Communications, 13(8):818–821, 2011.

Matthew A Hopcroft, William D Nix, and Thomas W Kenny. What is the young's modulus of silicon? Journal of microelectromechanical systems, 19(2):229–238, 2010.

Shan Huang, Feifei Fan, Ju Li, Sulin Zhang, and Ting Zhu. Stress generation during lithiation of high-capacity electrode particles in lithium ion batteries. Acta Materialia, 61(12):4354 – 4364, 2013. ISSN 1359-6454.

Zheng Jia and Teng Li. Intrinsic stress mitigation via elastic softening during two-step electrochemical lithiation of amorphous silicon. Journal of the Mechanics and Physics of Solids, 91:278 – 290, 2016. ISSN 0022-5096.

Zheng Jia and Wing Kam Liu. Analytical model on stress-regulated lithiation kinetics and fracture of si-c yolk-shell anodes for lithium-ion batteries. Journal of The Electrochemical Society, 163(6):A940, 2016.

Akihiro Kushima, Jian Yu Huang, and Ju Li. Quantitative fracture strength and plasticity measurements of lithiated silicon nanowires by in situ tem tensile experiments. ACS nano, 6(11):9425–9432, 2012.

Weiqun Li, Ke Cao, Hongtao Wang, Jiabin Liu, Limin Zhou, and Haimin Yao. Carbon coating may expedite the fracture of carbon-coated silicon core–shell nanoparticles during lithiation. Nanoscale, 8(9):5254–5259, 2016.

Xiao Hua Liu, He Zheng, Li Zhong, Shan Huang, Khim Karki, Li Qiang Zhang, Yang Liu, Akihiro Kushima, Wen Tao Liang, Jiang Wei Wang, et al. Anisotropic swelling and fracture of silicon nanowires during lithiation. Nano letters, 11(8):3312–3318, 2011.

Xiao Hua Liu, Jiang Wei Wang, Shan Huang, Feifei Fan, Xu Huang, Yang Liu, Sergiy Krylyuk, Jinkyoung Yoo, Shadi A Dayeh, Albert V Davydov, et al. In situ atomic-scale imaging of electrochemical lithiation in silicon. Nature nanotechnology, 7(11):749, 2012a.

Xiao Hua Liu, Li Zhong, Shan Huang, Scott X Mao, Ting Zhu, and Jian Yu Huang. Size-dependent fracture of silicon nanoparticles during lithiation. Acs Nano, 6(2):1522–1531, 2012b.

Wei Luo, Yunxiao Wang, Shulei Chou, Yanfei Xu, Wei Li, Biao Kong, Shi Xue Dou, Hua Kun Liu, and Jianping Yang. Critical thickness of phenolic resin-based carbon interfacial layer for improving long cycling stability of silicon nanoparticle anodes. Nano Energy, 27:255–264, 2016.

Matthew McDowell, Ill Ryu, Seok Woo Lee, Chongmin Wang, William Nix, and Yi Cui. Studying the kinetics of crystalline silicon nanoparticle lithiation with in situ transmission electron microscopy. Advanced Materials, 24(45):6034–6041, 2012.

Christian Miehe, Nikolas Apel, and Matthias Lambrecht. Anisotropic additive plasticity in the logarithmic strain space: modular kinematic formulation and implementation based on incremental minimization principles for standard materials. Computer Methods in Applied Mechanics and Engineering, 191(47):5383–5425, 2002.

Matt Pharr, Zhigang Suo, and Joost Vlassak. Variation of stress with charging rate due to strain-rate sensitivity of silicon electrodes of li-ion batteries. Journal of Power Sources, 270:569–575, 2014.

Michael Poluektov, Alexander Freidin, and Łukasz Figiel. Modelling stress-affected chemical reactions in non-linear viscoelastic solids with application to lithiation reaction in spherical si particles. International Journal of Engineering Science, 128:44–62, 2018.

Michael Poluektov, Alexander Freidin, et al. Micromechanical modelling of mechanochemical processes in heterogeneous materials. Modelling and Simulation in Materials Science and Engineering, 27(8):084005, 2019.

Yue Qi, Haibo Guo, Louis G Hector Jr, and Adam Timmons. Threefold increase in the young's modulus of graphite negative electrode during lithium intercalation. Journal of The Electrochemical Society, 157(5):A558, 2010.

Yue Qi, Louis G Hector Jr, Christine James, and Kwang Jin Kim. Lithium concentration dependent elastic properties of battery electrode materials from first principles calculations. Journal of The Electrochemical Society, 161(11):F3010, 2014.

WM Robertson and DJ Montgomery. Elastic modulus of isotopically-concentrated lithium. Physical Review, 117(2):440, 1960.

Mohamed El Bachir Seck, Mihail Gărăjeu, and Renaud Masson. Exact solutions for the effective nonlinear viscoelastic (or elasto-viscoplastic) behaviour of particulate composites under isotropic loading. European Journal of Mechanics-A/Solids, 72:223–234, 2018.

Vijay Sethuraman, Michael Chon, Maxwell Shimshak, Venkat Srinivasan, and Pradeep Guduru. In situ measurements of stress evolution in silicon thin films during electrochemical lithiation and delithiation. Journal of Power Sources, 195(15):5062–5066, 2010.

Zeinab Sadat Sheikholeslami, Mohammad Yousefi, Mohammad Imani, and Morteza Daliri Joupari. Low-temperature, chemical vapor deposition of thin-layer pyrolytic carbon coatings derived from camphor as a green precursor. Journal of Materials Science, 53(2): 959–976, 2018.

Vivek Shenoy, Priya Johari, and Yue Qi. Elastic softening of amorphous and crystalline li–si phases with increasing li concentration: A first-principles study. Journal of Power Sources, 195(19):6825–6830, 2010.

Hansinee Sitinamaluwa, Jawahar Nerkar, Mingchao Wang, Shanqing Zhang, and Cheng Yan. Deformation and failure mechanisms of electrochemically lithiated silicon thin films. RSC advances, 7(22):13487–13497, 2017.

Maria Stournara, Pradeep Guduru, and Vivek Shenoy. Elastic behavior of crystalline li–sn phases with increasing li concentration. Journal of Power Sources, 208:165–169, 2012.

Samuel Tardif, Ekaterina Pavlenko, Lucille Quazuguel, Maxime Boniface, Manuel Maréchal, Jean-Sébastien Micha, Laurent Gonon, Vincent Mareau, Gérard Gebel, Pascale Bayle-Guillemaud, et al. Operando raman spectroscopy and synchrotron x-ray diffraction of lithiation/delithiation in silicon nanoparticle anodes. ACS nano, 11(11):11306–11316, 2017.

Salman Tariq, Kavin Ammigan, Patrick Hurh, Ryan Schultz, P Liu, and J Shang. Li material testing-fermilab antiproton source lithium collection lens. In Proceedings of the 2003 particle accelerator conference, volume 3, pages 1452–1454. IEEE, 2003.

Haoran Wang and Huck Beng Chew. Molecular dynamics simulations of plasticity and cracking in lithiated silicon electrodes. Extreme Mechanics Letters, 9:503–513, 2016.

Rong Xu and Kejie Zhao. Mechanical interactions regulated kinetics and morphology of composite electrodes in li-ion batteries. Extreme Mechanics Letters, 8:13–21, 2016.

Zheng-Long Xu, Xianming Liu, Yongsong Luo, Limin Zhou, and Jang-Kyo Kim. Nanosilicon anodes for high performance rechargeable batteries. Progress in Materials Science, 90:1–44, 2017.

Hui Yang and Jianmin Qu. Fracture toughness of lixsi alloys in lithium ion battery. Extreme Mechanics Letters, 32:100555, 2019.

Hui Yang, Feifei Fan, Wentao Liang, Xu Guo, Ting Zhu, and Sulin Zhang. A chemo-mechanical model of lithiation in silicon. Journal of the Mechanics and Physics of Solids, 70:349–361, 2014.

Xiangchun Zhang, Wei Shyy, and Ann Marie Sastry. Numerical simulation of intercalation-induced stress in li-ion battery electrode particles. Journal of the Electrochemical Society, 154(10):A910–A916, 2007.

Kejie Zhao, Wei Wang, John Gregoire, Matt Pharr, Zhigang Suo, Joost Vlassak, and Efthimios Kaxiras. Lithium-assisted plastic deformation of silicon electrodes in lithium-ion batteries: a first-principles theoretical study. Nano letters, 11(7):2962–2967, 2011.

Kejie Zhao, Matt Pharr, Qiang Wan, Wei Wang, Efthimios Kaxiras, Joost Vlassak, and Zhigang Suo. Concurrent reaction and plasticity during initial lithiation of crystalline silicon in lithium-ion batteries. Journal of The Electrochemical Society, 159(3):A238–A243, 2012a.

Kejie Zhao, Georgios A. Tritsaris, Matt Pharr, Wei L. Wang, Onyekwelu Okeke, Zhigang Suo, Joost Vlassak, and Efthimios Kaxiras. Reactive flow in silicon electrodes assisted by the insertion of lithium. Nano Letters, 12(8):4397–4403, 2012b.